Published in final edited form as:

Nature. 2014 September 11; 513(7517): 261–265. doi:10.1038/nature13453.

Serial time-resolved crystallography of photosystem II using a femtosecond X-ray laser

A full list of authors and affiliations appears at the end of the article.

Abstract

Photosynthesis, a process catalysed by plants, algae and cyanobacteria converts sunlight to energy thus sustaining all higher life on Earth. Two large membrane protein complexes, photosystem I and II (PSI and PSII), act in series to catalyse the light-driven reactions in photosynthesis. PSII catalyses the light-driven water splitting process, which maintains the Earth's oxygenic atmosphere[1]. In this process, the oxygen-evolving complex (OEC) of PSII cycles through five states, S_0 to S_4, in which four electrons are sequentially extracted from the OEC in four light-driven charge-separation events. Here we describe time resolved experiments on PSII nano/microcrystals from Thermosynechococcus elongatus performed with the recently developed[2] technique of serial femtosecond crystallography. Structures have been determined from PSII in the dark S_1 state and after double laser excitation (putative S_3 state) at 5 and 5.5 Å resolution, respectively. The results provide evidence that PSII undergoes significant conformational changes

Correspondence and requests for materials should be addressed to P.F. (pfromme@asu.edu).
*These authors contributed equally to this work.

Supplementary Information is available in the online version of the paper.

Author Contributions C.K., I.G., R.F., M.S.H., R.L.S., A.R., K.S., G.J.W., S. Boutet, H.N.C., U.W., R.B.D., M.F., J.C.H.S. and P.F. contributed to the design of the experiment; C.K., I.G., K.N.R., J.-H.Y., D.E.C., B.R., C.E.C. and S.R.-C. worked on cell growth and photosystem II isolation; J.J.B., T.A.M. and A.L.M. worked on plastoquinone synthesis; C.K., I.G., K.N.R., D.E.C., B.R. and J.J.B. worked on biochemical and biophysical characterization of the photosystem II samples; C.K., K.M.D., L.Y. and Y.P. worked on EPR experiments to confirm the S_3 population; C.K., I.G., M.S.H., D.E.C. and P.F. developed nano/microcrystallization conditions of photosystem II; C.K., I.G., R.F., K.N.R., M.S.H. and D.E.C. grew crystals of photosystem II; C.K., I.G., R.F., K.N.R., J.-H.Y., D.E.C., R.G.S., H. Laksmono, M.J.B., T.-C.C. and P.F. conducted biophysical characterization of photosystem II crystals; C.K., I.G., L.G., M.L., L.L., J. Steinbrener, F.S. and P.F. designed and/or fabricated calibration or backup samples; C.K., I.G., D.W., D.J., D.D., U.W., R.B.D. and P.F. tested and optimized buffer and crystal suspension conditions for injection; D.W., D.J., D.D., R.A.K., U.W. and R.B.D. designed and produced nozzles; R.B.D., U.W., R.L.S., D.W., D.J., D.D., R.A.K., S. Bari. and L.L. developed and operated the injector; R.L.S., J. Steinbrener and L.L. developed and operated the sample delivery system and the anti-settling device; S. Boutet, M.M. and G.J.W. developed diffraction instrumentation; M.M., M.S., G.J.W. and S. Boutet set up and operated the CXI beamline; M.S.H., R.A.K., D.M., S. Boutet, M.F. and P.F. designed and optimized the laser excitation scheme and aligned the lasers; C.K., S. Basu., I.G., R.F., N.A.Z., M.S.H., R.L.S., T.A.W., D.W., D.J., D.E.C., H.F., H. Laskmono, H. Liu, A.B., A.L.A., D.D., R.A.K., S. Bari., K.R.B., M.J.B., T.-C.C., L.G., S.K., C.C., M.L., M.M., K.N., M.S., J. Steinbrener, F.S., C.Y., G.J.W., S. Boutet, H.N.C., U.W., R.B.D., M.F., J.C.H.S. and P.F. collected X-ray diffraction data at the CXI beamline; S. Basu, R.F., N.A.Z., T.A.W., H. Liu, A.B., A.L.A., R.A.K., K.R.B., S.K., K.N., L.G., C.Y., J.C.H.S. and P.F. analysed the femtosecond crystallography X-ray diffraction data; T.A.W., A.B., A.L.A., R.A.K. and H.N.C. developed the data evaluation and/or hit finding programs; S. Basu, R.F. and N.A.Z. merged the 3D data; S. Basu and R.F. refined the structure and calculated the electron density maps; S. Basu, R.F., N.A.Z. and P.F. designed and made the figures; R.L.S., T.A.W., D.W., D.J., R.L.S., A.B., A.L.A., A.R., K.S., S.M., A.V.M., S.P.H.-R., R.G.S., H.N.C., U.W., R.B.D., M.F., J.C.H.S., T.A.M. and A.L.M. contributed to the writing of the manuscript with discussion, comments or edits; C.K., S. Basu, R.F., N.A.Z., K.N.R., H.N.C., M.F., J.C.H.S. and P.F. contributed to the interpretation of the results; C.K., S. Basu, I.G., R.F., N.A.Z., K.N.R., C.E.C., H.N.C., U.W., R.B.D., M.F., S.R.-C., J.C.H.S. and P.F. wrote and edited the manuscript with discussion and input from all authors.

The structure factors and coordinates have been deposited in the Protein Data Bank and accession codes for S_1 and putative S_3 states are 4PBU and 4Q54, respectively.

The authors declare no competing financial interests.

at the electron acceptor side and at the Mn_4CaO_5 core of the OEC. These include an elongation of the metal cluster, accompanied by changes in the protein environment, which could allow for binding of the second substrate water molecule between the more distant protruding Mn (referred to as the 'dangler' Mn) and the Mn_3CaO_x cubane in the S_2 to S_3 transition, as predicted by spectroscopic and computational studies[3,4]. This work shows the great potential for time-resolved serial femtosecond crystallography for investigation of catalytic processes in biomolecules.

The first X-ray structure of PSII was determined to a resolution of 3.8 Å in 2001 (ref. 5) revealing the protein's architecture and the overall shape and location of the OEC. In 2011, Shen and co-workers achieved a breakthrough in the structural elucidation by dramatically improving crystal quality, enabling determination at 1.9 Å resolution[6]. This structure showed the OEC at near atomic resolution. However, the OEC was probably affected by X-ray damage, a fundamental problem in X-ray crystallography.

The X-ray damage problem may be overcome through the use of serial femtosecond crystallography (SFX)[2,7,8], an advance enabled by the advent of the X-ray free electron laser (XFEL). In SFX, a stream of microcrystals in their mother liquor is exposed to intense 120 Hz femtosecond XFEL pulses, thereby collecting millions of X-ray diffraction 'snapshots' in a time-frame of hours. Each X-ray FEL pulse is so intense that it destroys the sample; however, the pulse duration is so short that diffraction is observed before destruction occurs[9].

Conventional X-ray structures correspond to a temporal and spatially averaged representation of biomolecules, leading to a 'static' picture. To capture dynamic processes such as water oxidation in PSII, time-resolved X-ray data can be collected using SFX[10–12]. Conformational changes may be observed at a time-resolution ranging from femtoseconds to microseconds by combining visible laser excitation with the SFX setup and varying time delays between the optical pump and the X-ray probe snapshot. As partial reflections from crystals in random orientations are recorded, many snapshots must be collected for adequate sampling of the full reflections and three-dimensional reconstruction. A time-resolved pump-probe experiment was performed in 2010 using PSI-ferredoxin crystals as a model system, in which changes in diffraction intensities, consistent with a light-induced electron transfer process in the PSI-ferredoxin complex and dissociation of the PSI-ferredoxin complex were seen[10].

The catalytic reaction in PSII is a dynamic process. The oxygen evolution reaction is catalysed by the oxygen-evolving complex (OEC), in which the electrons are extracted from the OEC in four sequential charge separation events through the S-state cycle (Kok cycle), as shown in Fig. 1a (see ref. 1 for a review). SFX diffraction and X-ray emission spectroscopy (XES) were reported investigating the dark S_1 state and the single flash (S_2 state) of PSII[13]. The XES data show that the electronic structure of the highly radiation sensitive Mn_4CaO_5 cluster does not change during femtosecond X-ray exposure[13]. However, the quantity and quality of X-ray diffraction data was insufficient to determine if any structural changes occurred.

We report on microsecond time-resolved SFX experiments conducted at the CXI instrument[14] at the Linac Coherent Light Source (LCLS)[15]. The experimental setup is shown in Fig. 1b, c. We developed a multiple-laser illumination scheme that progressively excites the OEC in dark-adapted PSII nano/microcrystals by two laser pulses from the dark S_1 state via the S_2 state to the double-flash putative S_3 state. Not all PSII centres progress to the next S-state by a single saturating flash which could lead to heterogeneities. Therefore the S-state reached in the double-flash experiment is indicated as 'putative S_3 state' here.

The diffraction patterns collected from dark and illuminated crystals were sorted into two data sets. Using the 'hit finding' program Cheetah[16], 71,628 PSII diffraction images were identified from the dark diffraction patterns and 63,363 were identified from the double-flash patterns, see Extended Data Fig. 2 for examples. From these hits, 34,554 dark state patterns and 18,772 double-flash patterns were indexed and merged to reduce all stochastic errors using the CrystFEL software suite[17] (see Extended Data Table 2a, b). The data were indexed as orthorhombic, with unit-cell parameters of a = 133 Å, b = 226 Å, and c = 307 Å for the dark state, and a = 137 Å, b = 228 Å, and c = 309 Å for the double-flash state (for error margins see Table 1). The distributions of unit cell dimensions are shown in Extended Data Fig. 3 and Extended Data Table 2a, b. The data clearly supports an increase in unit cell dimensions in the double-flash state, with the largest difference detected for the a axis. Two factors may explain the change in unit cell constants, lower indexing rates and a slight decrease in resolution of diffraction: crystal degradation upon laser illumination or significant structural changes upon the transition from the dark state to the double-flash state, which may represent the putative S_1 to S_3 transition. To distinguish between these two possibilities, we collected data with triple-flash excitation of the PSII crystals, where at least part of the PSII centres may have reached the putative transient S_4 state. Preliminary data evaluation of the triple-flash data set (that is, putative S_4 state) shows similar unit cell dimensions and crystal quality as the dark S_1 state (see Extended Data Fig. 3 and Extended Data Table 2a). This suggests that conformational changes induced in PSII by the double-flash excitation (that is, during the putative S_1 to S_3 transition) are reversed after excitation with the third flash (in the putative S_3 to S_4 transition), as discussed in the Methods.

Diffraction data from the dark and double-flash states were evaluated to 5 Å and 5.5 Å resolution, respectively; the data refinement statistics are shown in Table 1. As each diffraction pattern represents a thin cut through reciprocal space by the Ewald sphere, only partial reflections were recorded. A high multiplicity of observations is therefore needed for each Bragg reflection to obtain full, accurate structure factors. The average multiplicity per reflection was 617 for the dark state data set and 383 for the double-flash data set over the whole resolution range (see Extended Data Tables 1a, b). Extended Data Table 2c shows a comparison of the data statistics of this work with the S_1 and S_2 data in ref. 13.

The data were phased by molecular replacement using a truncated version of the 1.9 Å structure (PDB accession code 3ARC)[6]. Rigid body refinement (phenix.refine) was performed for both the dark and double-flash structures (see Methods for further details on molecular replacement and refinement). To reduce model bias, we calculated omit maps and simulated annealed maps (SA-omit maps) for the dark and double-flash data, deleting the coordinates of the Mn_4CaO_5 cluster from the model.

Figure 2a–c shows the arrangement of protein subunits and cofactors of photosystem II, including the electron transport chain. The comparison of the electron density maps for the dark state (green) and the double-flash state (white) at a contour level of 1.5 σ is shown in Fig. 2d–f. Both maps show clear electron densities for the transmembrane helices as well as loops and cofactors. Additional electron density maps for representative structural elements of PSII are shown in Extended Data Figs 5, 6, 7 and 8. Overall, the protein fits into the electron densities for the dark and double-flash states and matches with the high resolution structural model. However, differences appear in regions of the Mn_4CaO_5 cluster and the acceptor side, where the quinones and the non-haem iron are located. Determining the significance of these changes and their correlations is complicated due to the resolution limit of the data. Figure 2g–i shows detailed views of the loops at the acceptor side of PSII. The quinones are not visible at the current resolution of 5 Å. The maps indicate differences between the electron densities of the dark and double-flash states in the loop regions and also in the position of the non-haem iron that is coordinated by the loops.

We now focus on the structure in the undamaged dark S_1 state of the metal cluster in the OEC and the potential light-induced structural changes that may occur during the S-state transition. Extended Data Fig. 8 shows the SA-omit map of the OEC in the dark S_1 state for the Mn cluster in PSII with the 1.9 Å X-ray structure in ref. 6. Interestingly, the electron-density map of the dangler Mn atom from the 1.9 Å structure is located outside the dark S_1 state electron density, a feature also visible in the electron density map of ref. 13. These structural observations are consistent with spectroscopic results, which indicate that the distance between the dangler Mn and the Mn_3O_xCa distorted cubane is indeed shorter in the dark S_1 state than in the 1.9 Å structure based on the synchrotron data, which might be influenced by X-ray induced reduction of the Mn ions in the metal cluster[18,19]. This shorter distance is in agreement with density function theory (DFT) studies[4,18,20] based on the 1.9 Å structure of PSII[6], however, the current resolution limit of 5 Å does not allow a quantitative assessment.

The mechanism of water splitting is intensely debated and many models have been proposed. The recent 1.9 Å X-ray structure[6] formed the basis for more detailed theoretical studies of the process, yet the proposed mechanisms differ[4,20–22]. Based on our time-resolved SFX (TR-SFX) structural data, we looked for differences between the electron-density maps of the OEC, derived from the dark and the double-flash datasets. Figure 3a, b shows the SA-omit maps calculated for dark (blue) and double-flash state (yellow) and compared with the model of the metal cluster from the 1.9 Å structure[6] (Fig. 3c). The Mn_4CaO_5 cluster was omitted from the model for the calculation of the SA-omit map, which is based on annealing at a virtual temperature of 5000 K to minimize phase bias. The SA-omit electron densities of the dark and double-flash states differ in the shape and position, as well as in the protein environment, of the Mn_4CaO_5 cluster. The dark state simulated-annealed (SA)-omit electron density for the OEC protein environment matches the model of the 1.9 Å structure[6], whereas the SA-omit map of the double-flash state differs significantly. Any interpretation of changes in the protein environment of the OEC is highly speculative at a resolution of 5 Å and heterogeneities in the S-state transitions. However, the SA-omit map of the double-flash state is suggestive of conformational changes which may indicate a movement of the CD loop (including the ligand D170) away from the cluster. If confirmed at

higher resolution, this could explain mutagenesis studies that raised questions about the ligand-role of D170 in the higher S-states[23]. Furthermore, in the double-flash state, the electron density of the metal cluster extends and shows a new connection to the AB loop at the site where D61 is located. Although D61 only serves as a second sphere ligand in the 1.9 Å crystal structure[6], mutagenesis studies indicated an important role in the water oxidation process, as the S_2 to S_3 transition is blocked in D61 mutants.

The change in the electron-density of the OEC is suggestive of an increase in the distance between the cubane and the dangler Mn and distortion in the cubane in the double-flash state. The observed electron densities (Fig. 3a, b) of the dark state and double-flash state are consistent with conformational changes predicted in a recent DFT study of the S_3 state in ref. 4, shown in Fig. 3d. The increased distance between the cubane and dangler Mn could allow the second 'substrate' water molecule to bind between the Mn_3O_xCa cubane and the dangler Mn in the S_2 to S_3 state transition. It was shown by extended X-ray absorption fine structure (EXFAS) spectroscopy that the Mn–Ca^{2+} distances in the Mn_3O_xCa cubane shrink in the S_3 state[24]. Although the Jahn-Teller effect extends the distances between metals in the lower S-states of the OEC (Mn oxidation states +II, +III and +IV), a shrinking of the Mn_3O_xCa cubane is predicted in the S_3 state when all 4 Mn in the OEC have reached the oxidation state +IV. A comparison of the electron density in the dark and the double-flash states may indeed suggest an overall decrease in the dimension of the Mn_3O_xCa cubane in the double-flash state, which is in good agreement with the proposed S_3 state EXAFS and XES models[25] (more detail provided in the Supplementary Discussion). The consistency of spectroscopy and DFT studies with our observations may provide preliminary indications that a significant fraction of the OEC centres in our crystals have reached the S_3 state in the double-flash experiment.

Our time-resolved SFX study captures the image of PSII after it has been excited by 2 saturating flashes and provides experimental evidence for structural changes occurring in the putative S_3 state of the OEC, accompanied by structural changes at the acceptor side of PSII. As the resolution is limited to 5 Å, the interpretation of the changes observed is preliminary. This work is a proof-of-principle that time-resolved SFX can unravel conformational changes at moderate resolution and may lay the foundation for solving high resolution structures of PSII at all stages of the water oxidation process in the future. To unlock the secrets of the water-splitting mechanism by TR-SFX at atomic detail, the resolution must be further improved and structures must be determined from all the S-states with multiple time delays.

METHODS

Isolation and crystallization of photosystem II

Photosystem II (PSII) was isolated from *Thermosynechococcus elongatus* as described in ref. 32 with the following modifications. The samples were frozen after the ion exchange chromatography step and batch precipitation/crystallization of PSII was performed four times in decreasing concentrations of PEG 2000, the last purification step was performed at LCLS directly before growth of microcrystals.

Standard crystallization methods, such as vapour diffusion and hanging drop, have become the dominant techniques for the growth of protein crystals in the past decade. These methods have been optimized for very small volumes of protein that are currently not useful for serial femtosecond crystallography (SFX). Batch crystallization has been successfully used for the growth of large PSII crystals for standard crystallography[32] and crystallization in batch method can be easily scaled up for large protein volumes. Growth of very small PSII crystals (approximately 1 μm) using the batch method, at high yield, requires high super-saturation conditions to enhance nucleation. This leads to a very broad size distribution of crystals, visible crystal defects, and a coexistence of crystals and amorphous precipitate.

The growth of PSII microcrystals for data collection was performed using a free interface diffusion technique that had been adapted to a batch method for a higher yield. In this approach, nucleation is initiated at the interface between the high density precipitant solution and the lower density protein solution, containing PSII detergent micelles. The protein solution was prepared by dissolving the PSII precipitate from the fourth precipitation step (see above) in solubilisation buffer A-sol (100 mM PIPES pH7.0, 5 mM $CaCl_2$, 10 mM tocopherol, 0.03% β-dodecylmaltoside (DDM) (from glycon >99.9% purity), adjusting the concentration of chlorophyll (chl) to 0.5 mM. The crystals were grown in batch experiments in 15 ml Falcon tubes by adding precipitation buffer to a final concentration of 100 mM PIPES pH 7.0, 5 mM $CaCl_2$, 10 mM tocopherol, and 10–17% PEG 2000 to the protein solution. The optimal PEG and protein concentration was experimentally determined for each protein batch separately, in small-scale experiments, before the remainder of the protein was crystallized on site at LCLS directly before data collection. All precipitation steps and the crystallization were carried out in darkness to avoid pre-illumination of the crystals. The PEG precipitant solution was added to the PSII solution at a rate of approximately 20 μl per second. The slow addition of the PEG precipitant, with a higher density than the protein solution, led to a two-phase system, where the precipitant solution gathered at the bottom of the tube with a small mixed zone in between the top protein layer and the bottom PEG layer. Once the crystals formed and reached a sufficient size, they sedimented into the precipitant solution and formed a pellet at the bottom of the tube. As the precipitant solution did not contain protein, the crystal growth stopped (see Extended Data Fig. 1a–e). To further ensure that crystal growth had been terminated, the supernatant was removed after 48 h and a stabilization buffer (100 mM PIPES pH7.0, 5 mM $CaCl_2$, 10 mM tocopherol, 20% PEG 2000) was added. This buffer also served as the running buffer for delivery of the crystals to the X-ray interaction region during the time-resolved serial femtosecond crystallography (TR-SFX) experiments. The supernatant was saved and later used once crystals reached sufficient size, as it continued to crystallize at a significantly slower rate, due to the decreased protein concentration. The crystallization progress was monitored closely by taking 1 μl samples at regular intervals to determine crystal size by dynamic light scattering (DLS) (see Extended Data Fig. 1d). Crystals were collected and directly used for the SFX experiments after they reached a size of around 1 μm. Although DLS provides the size distribution of the particles, it cannot discriminate between amorphous and crystalline particles. The crystallinity of the samples was therefore monitored by SONICC, which detects nanocrystals as small as 100 nm[26]. Extended Data Fig. 1a–e show the crystallization method and results of crystal characterization experiments.

All handling steps with the crystals were performed in dim green light to limit exposure. After growth and stabilization, crystals were stored in complete darkness. All steps thereafter were done in the dark.

The plastoquinone derivative PQ_{decyl} was not added to the crystals until the beamtime in June 2012 and therefore was not a part of the double-flash (that is, putative S_3) experiments. J. Bergkamp synthesized PQ_{decyl} in the laboratories of A. L. Moore and T. A. Moore at Arizona State University. It contains the same head group as plastoquinone but the 15 units of the isoprene tail were replaced by an *N*-decyl chain to improve solubility. We have independently determined that addition of PQ_{decyl} maintains full oxygen evolving activity of PSII under continuous illumination for several minutes. A plastoquinone molecule is located in the quinone binding pocket Q_B in S_1, after two laser excitation flashes, reaching the putative S_3 state, the natural plastoquinone (PQ) becomes double reduced to PQ^{2-}, which takes up two protons and leaves the binding site as plastoquinol PQH_2. The empty binding pocket is then re-populated by PQ_{decyl}, before the third laser flash induces the next charge separation event to reach the S_4 state (see Fig. 1a for the S-state scheme[31] that also features the reduction state of the quinone in each of the S-states).

Characterization of microcrystals by SONICC and DLS

All crystal samples were characterized via two methods, second order nonlinear imaging of chiral crystals (SONICC)[26]. The SONICC and DLS experiments were performed using 24-well VDXm plates for data collection from 1 μl suspension of the crystals. The reservoir was filled with 500 μl of precipitation buffer to prevent evaporation of the 1 μl hanging drop containing the crystals. The crystals were monitored by the SONICC system, at 200 mW laser power for an exposure time of 1 s. In the SONICC technique, the crystals were excited by two femtosecond infrared laser pulses of 1064 nm leading to second harmonic generation. The SONICC signal was detected at 532 nm. The dynamic light-scattering experiments were performed in 1 μl hanging drops. Our DLS instrument is equipped with an infrared laser at 785 nm to avoid excitation of the pigments in PSII during the measurements. Attempts to conduct DLS measurements on PSII samples with a red laser, as used in most commercial DLS instruments, failed due to the strong absorption of red light by the chlorophylls in PSII, which strongly diminished the signal. For each sample, 10 measurements were performed with 20 s of data collection per measurement. The viscosity of the buffer solutions was determined experimentally by calibration with 140 nm polystyrene beads. The crystal size distribution was found to be around 1 μm (see Extended Data Fig. 1d).

EPR characterization of the S-state transition

Electron paramagnetic resonance (EPR) has been used extensively to determine the progression of PSII through the S-state cycle[33,34]. Using this technique, quantification of the S_2 state is determined by the multiline signal (MLS), a signature of only this state of PSII. Protein solutions, used for PSII crystallization, were cycled through the S-states by multiple single flash laser excitation (1–3 flashes) at room temperature. The samples were flash frozen directly after laser excitation in liquid nitrogen and the yield of multiline signal was interrogated by EPR at low temperature. The EPR experiments were performed under

conditions that were as similar as possible but not identical to the LCLS experiments (for example the EPR data collection required freezing in glycerol, whereas SFX data are collected at room temperature without glycerol addition). As the S-state yield is an estimate, the double-flash state is indicated as 'putative S_3 state' here. Prior to illumination, glycerol was added to samples as a cryo-protectant, yielding a final concentration of ~30% by volume. This resulted in a final PSII concentration of 1.8 mg chlorophyll per ml (2 mM). Dark adaption was performed before the EPR experiments, therefore the PSII samples were initially, predominately in the S_1 state. We did not attempt to get all the PSII into the S_1 state, using pre-illumination flashes in the presence of artificial electron acceptors followed by dark adaptation (as described in ref. 34) as the natural mobile plastoquinone (1 Q_B per reaction centre)would leave the binding site and consequently be lost in the pre-illumination phase.

For flash illumination at room temperature (20 °C), a Continuum Surelite EX Nd: YAG laser was used with a second harmonic generator yielding 532 nm, 8 ns, 1 Hz, and ~380 mJ (fluence of ~10^3 mJ per cm^2) pulses. Low-temperature X-band EPR spectra of the flash-frozen samples were recorded using a Bruker EMX X-band spectrometer equipped with a X-Band CW microwave bridge. The sample temperature was maintained at 10 K by an Air Products LTR liquid helium cryostat during collection of the EPR spectra. Spectrometer conditions were as follows: microwave frequency, 9.48 GHz; field modulation amplitude, 25 G at 100 kHz; microwave power, 31 mW.

Dark-adapted samples of both PSII solutions and crystal suspensions (frozen without illumination) contained a small percentage (typically 10%) of multiline signal. To determine the maximal possible yield of the MLS, the dark adapted, frozen PSII samples were illuminated at 190 K (dry ice/ethanol bath) for 20 min. The S-state cycle stops at the S_2 state at low temperature (190 K)[33], therefore all photoactive PSII reaction centres can be brought into the S_2 state by low temperature continuous illumination. The illumination of the frozen crystal suspensions was performed in 2-min intervals with the maximum MLS signal intensity achieved within the first 2 min of continuous illumination. We observed that the presence of glycerol affects the intensity of the MLS. Solutions and crystals to which no glycerol was added exhibited lower MLS intensity after continuous illuminations.

Extended Data Fig. 1f shows the EPR spectra of PSII samples, which were excited by 1 or 2 laser flashes at room temperature, followed by flash freezing in the dark. In addition, the graph also shows the control experiment in which dark-adapted frozen PSII was continuously illuminated at 190 K to achieve the maximal S_2 yield. A miss parameter α = 9.7% was obtained by fitting the MLS intensities as a function of laser flashes, see Extended Data Fig. 1g. Samples exposed to three flashes were also included. The data evaluation indicates that with two flash illuminations at least 70%of the PSII reaction centres have reached the S_3 state under these conditions.

The transition rates are comparable to results of EPR studies on spinach PSII by Styring *et al.*, who published transition rates of maximum 75% under conditions that were highly optimized for maximal yields of S-state transitions[34].

CXI instrument setup and sample delivery for TR-SFX data collection on PSII crystals in the double-flash state

TR-SFX data were collected at the Coherent X-ray Imaging (CXI) instrument[14] at the Linac Coherent Light Source (LCLS)[15] at SLAC National Accelerator Laboratory (for reviews on TR-SFX see refs 11, 12). The PSII crystals were delivered to the interaction region with the FEL beam as a suspension of crystals using the gas focusing liquid injector described in refs 27, 35, 36. The injection process was improved by the invention of an anti-settling device[37], which also was modified to permit temperature control of the sample. Stainless steel syringes containing the crystal suspension (pre-filtered through 10 μm stainless steel filters from IDEX) were mounted on a rotating holder, which was cooled with a Peltier element to 10 °C. This set-up maintained the crystals at their growth-temperature until their delivery to the FEL interaction region by the gas focusing jet. The glass capillary nozzle tips were polished to allow for visible laser excitation of the crystals in the nozzle tip. A black coating upstream of the nozzle tip prevented pre-excitation of the crystal suspension upstream of the optical laser interaction region. The gas focused liquid jet had a diameter of 4 μm at the intersection with the X-ray focal area of 2 μm^2 full width at half maximum (FWHM) using the CXI instrument. Data were collected at the X-ray photon energy of 6.0 keV (2.05 Å) with an X-ray pulse duration of approximately 50 femtoseconds. The X-ray diffraction patterns were detected on a Cornell-SLAC Pixel Array Detector (CSPAD)[38,39]. The detector consisted of 64 panels, each 194 × 185 pixels tiled to span approximately 1728 × 1728 pixels with gaps between the tiles and approximately 19 cm along one side.

Double laser excitation of photosystem II crystals

PSII was excited by two subsequent optical pump-laser pulses from a diode-pumped, frequency-doubled Nd: YLF laser (Evolution-30, Coherent), emitting visible laser pulses at a wavelength of 527 nm. The laser was fibre-coupled from a table outside the experimental chamber, channelled into the chamber and onto the head of the liquid jet injector[27,35]. This wavelength provided a good compromise between transmission and absorption of light in the PSII crystals to ensure approximately homogeneous excitation throughout the crystals (the size of crystals was approximately 1 μm), as identified by DLS (see Extended Data Fig. 1d). The optical double pulse was produced by an active Q-switch with ‘on times’ chosen such that the pulse energies of both laser pulses match. This resulted in pulse lengths of 90 ns and 150 ns for the first and second pulses, respectively, this was done to maintain the total number of photons incident on the crystal same. The laser was focused to an area of approximately 400 μm in diameter with a flat top profile and aimed at the transparent tip of the nozzle, about 100 μm upstream from the X-ray interaction region. The laser beam diameter and aim point were chosen based on the desired pump-probe delays and calculations of sample flow profile and flow speed inside the capillary (average speed of 85 mm per second for 50 μm inner diameter of the nozzle) and in the jet (12 m per second for the 4 μm jet). This allowed for illumination of the crystals at the tip of the nozzle and in the liquid jet. It also ensured that crystals probed by X-rays were first exposed to both optical laser pulses for the ‘pumped’ measurements (see Fig. 1b, c). The molar extinction coefficient was determined from dissolved PSII crystals at 527 nm, which was then used to calculate the absorption of PSII crystals with approximately 1 μm path length. From these parameters, it was calculated that a minimum fluence of 2.3 mJ per cm^2 (or a pulse energy

of 3 μJ for a 400 μm diameter spot) was required to excite every PSII complex in a crystal of 1–2 μm diameter.

During the experiment, the laser pulse energy was monitored using a power meter placed at a 50:50 beam splitter on the laser table (50% of the energy going into the experiment). The energy of the laser pulse transmitted to the sample was calculated by the previously measured transmission of the entire fibre setup from the 50:50 beam splitter to the final lens in the injector (including fibre couplings and feed-through) and using 20% as a conservative estimate for the light transmission through the optically transparent end of the nozzle to the sample. That transmission could not be measured directly, so it was indirectly estimated. The laser pulse energy was chosen to correspond to approximately 6 μJ per pulse at the sample, that is, three times what is required to optimally pump a 1–2 μm PSII crystal at 527 nm[34]. The desired timing of the optical laser pulses with respect to the X-ray pulses from LCLS[15] were achieved by using the LCLS/CXI event generator and event reader (EVG/EVR) system that provided precise timing signals less than 1 μs before every X-ray pulse (or every other X-ray pulse) and a SRS DG645 delay generator to produce properly timed double trigger signals for the laser Q switch. The time-delay between the two optical laser pulses was set to be 210 μs corresponding to three times the time constant for the S_1 to S_2 transition of 70 μs[28]. The time delay between the second optical pulse and the X-ray pulse was 570 μs to allow the oxygen-evolving complex (OEC) to complete the S_2 to S_3 transition (3 times the time constant of 190 μs for the S_2 to S_3 transition)[28]. As the electron transfer between Q_A to Q_B takes place in the 200 to 400 μs time range[40], (depending also on the organism and oxidation state of Q_B) the delay time of 780 μs between flash 1 and the X-ray pulse represents a reasonable minimal delay time aimed at following both the processes at the donor side in the OEC and the acceptor side at the Q_B binding site. The uniform change in unit-cell dimension in the double-flash experiment (putative S_3 state) and its reversion in the triple flash experiment (putative transient S_4 state) provides an independent indication for significant and uniform progression of the OEC through the S-states.

In order to monitor the delay between the pump beam and the probe beam, we separately measured the response of two photodiodes to the optical and X-ray excitation with an Acqiris digitizer. One photodiode was exposed to stray optical light on the laser table and the other to X-rays scattered from the sample jet at very high angle. This was necessary because of the disparity in the response of the diodes to each signal near the interaction region—that is, at the required optical and X-ray fluences needed to perform the experiment, the signals could not be discriminated when using a single photodiode. The delay between the signals introduced by the measurement of the optical light on the laser table was measured at the beginning of the experiment by equalizing the signals from each beam near the X-ray interaction point. That constant was used to calculate a calibrated delay time with sufficient precision for our experiment using the digitizer trace.

The LCLS timing signal triggered the preceding optical laser pulses for every other X-ray pulse allowing us to acquire alternating diffraction images from ‘dark’ (ground state) and ‘double-flash’ PSII crystals in the putative S_3 state, that is, SFX data were collected with a frequency of the X-ray pulses of 120 Hz whereas the frequency of the pumplaser pulses was 60 Hz (Fig. 1b, c). This approach minimizes other sources of error that might occur from

systematic error. With this setup, alternating ‘dark’ and double excited ‘illuminated’ images were collected at 3,600 dark images and 3,600 illuminated images per minute. In addition to this alternating experimental scheme, dark run data was collected while the 527 nm pump laser was switched off (see Extended Data Table 2b for data statistics of dark only and alternate dark/light runs). Representative diffraction patterns of the S_1 and the double-flash data sets are shown in Extended Data Fig. 2a, b.

Processing and evaluation of data with the Cheetah and CrystFEL programs

A total of 5,528,071 raw diffraction frames were collected from photosystem II microcrystals in January 2012. The raw diffraction data (XTC format) were pre-processed by the Cheetah software package[16], and then analysed in the software suite CrystFEL[17]. Examples of diffraction patterns of the PSII crystals are shown in Extended Data Fig. 2a for the dark (S_1) state and in Extended Data Fig. 2b for the double-flash (putative S_3) state.

The first step of pre-processing involved dark current subtraction from each diffraction frame and masking of dead, hot, cold and saturated pixels. It also included masking of the low-resolution scattering from the liquid jet and the detector panel edges. Local background correction step was applied to the raw diffraction frames during their pre-processing in Cheetah[16]. Each diffraction frame was analysed and identified as a crystal ‘hit’ only if it contained 25 or more peaks with the intensities of at least 400 analogue-to-digital units. The locally background-corrected patterns collected in the alternating mode were sorted into two data sets for the dark and double-pumped hits based on signals from a photodiode and video camera in the experimental chamber. Comparison between the dark data sets from the alternating light/dark runs and complete dark runs showed no difference in unit cell constants, or indexing rates, therefore the dark data sets were merged. The final data sets contained 71,628 ‘hits’ from the dark state data set and 63,363 ‘hits’ from double-flash data sets. The triple-flash data sets, leading to the putative transient S_4 state of PSII (collected during a separate beamtime in June 2012), were collected in alternate runs with the frequency of 120 Hz of the LCLS X-ray pulses and 60 Hz laser excitation frequency. The same laser excitation scheme as described before was used to reach the S_4 state. The third laser excitation, reaching the S_4 state, was achieved by triggering a third laser excitation 527 nm laser pulse 570 μs after the second laser excitation pulse. This third pulse was triggered by a second 527 nm laser installed in the CXI hutch, which excited the jet through a separate hole in the shroud. The delay time between the third laser flash and the FEL X-ray pulse was 250 μs. The data sets from the January 2012 beamtime are designated as dark (A) and double-flash (A) and the data sets from the June 2012 beamtime are designated as dark (B) and triple-flash (B) (see Extended Data Table 2a). The dark (B) and triple-flash (B) data sets contained 33,373 and 32,190 hits, respectively. The hits for all data sets were passed as separate sets to the CrystFEL software suite[17] for auto indexing with MOSFLM, using the orthorhombic unit cell dimensions of PSII from *Thermosynechococcus elongatus* (PDB code 1FE1)[5] within a tolerance limit of 6%, 5%, 5% for the reciprocal axes of *a*, *b*, *c* respectively for the S_1 state. Similarly, the tolerance limit of8%,5%, 5%were used for the reciprocal axes of *a*, *b*, *c*, respectively, for the double-flash and triple-flash states. After indexing, the 4 data sets were handled separately and the ‘indexing rates’ (fraction of hits which could be successfully indexed) were 48% for dark (A), 29% for double-flash (A),

35% for dark (B), and 39% for triple-flash (B). Extended Data Table 2a, b shows the indexing statistics as well as the unit cell constants for all 4 data sets. The unit cell is orthorhombic and shows very significant changes in the unit cell dimensions between the dark S_1 and double-flash data sets (A) state (see Extended Data Table 2 and Extended Data Fig. 3). The most pronounced change is in the dimension of the a axis which increases by 3.3 Å. This change in unit cell constants is accompanied by the slight decrease in diffraction quality (5 vs 5.5 Å resolution) (see Extended Data Tables 1 and 2) and significant lowering of indexing rates. This change in the unit cell dimension is fully reversed to the unit cell constants observed in the dark S_1 state when PSII crystals are excited by three laser flashes, eventually reaching the putative transient S_4 state. Furthermore, the indexing rate for the dark (B) and triple-flash (B) data sets are comparable, with 35% and 39%, respectively.

Multiplicity in the measurements is very important due to the partial nature of all reflections, the variation of the flux in each FEL pulse and the fact that each diffraction pattern is collected from a different crystal. The triple-flash data set, with 12,500 diffraction patterns, is sufficient to accurately determine the unit cell constants. However, this is borderline for the determination of accurate structure factors and therefore, further data evaluation has been limited to the dark (S_1) and double-flash data sets.

The dark (S_1) and double-flash (putative S_3) data sets that were used for structure factor determination consist of 34,554 and 18,772 indexed patterns, respectively. Our data sets were merged separately in three dimensions and the structure factors were extracted separately from dark and double-flash data sets of PSII protein using the Monte Carlo method[41], which integrates the snapshots partial reflections from randomly oriented crystals of varying size and shape (see Supplementary Videos 1 and 2 for a graphical representation of the structure factor amplitudes of the both data sets). Average multiplicities are 684 and 373 in all resolution shells from 19.20 Å to 4.03 Å of the dark (S_1) and double-flash states, respectively (see Extended Data Tables 1a, b).

A comparison of the data statistics of our work with that of Kern *et al.* (ref. 13) is shown in Extended Data Table 2c. Our data sets evaluated with CrystFEL[17] show significantly higher multiplicity of the data and better correlation coefficients ($CC_{1/2}$)[29] which are indicative of the quality of the merged reflections, when compared to the data of Kern *et al* (ref. 13), evaluated with the software suite cctbx.xfel[30].

The internal consistency of the SFX data are expressed as R_{split}[17]. For the calculation of R_{split}, the sets of images of a data set are split into two random halves, and the structure factors are calculated separately for each half. The difference between the amplitudes of each of the structure factors of (hkl) plane between the two half data sets is used to estimate the convergence of the full data set as given by R_{split}. An R_{split} of 0.22 means an estimated 22% error of the structure factors of the full data set to the ‘true’ data set. The two half data sets would have agreed to 0.22 * sqrt(2).

R_{split} was calculated for the dark and double-pumped data sets separately. As expected, with an increasing number of indexed patterns, R_{split} decreases as the data set reaches higher

multiplicity and completeness (see Extended Data Fig. 4). The average R_{split} values over all resolution shells were 0.07 for the dark and 0.09 for the double-pumped data sets.

Structure determination

The data for the dark (S_1) and double-flash (that is, putative S_3) state of PSII were handled as two completely separate data sets for the whole data analysis process. After processing the raw serial femtosecond X-ray crystallographic data, the final structure factors from dark and double-pumped data sets were passed to the CCP4 software package[42].

Molecular replacement

Molecular replacement[43] was carried out by the PhaserMR program, which is a part of the CCP4 suite[42] using the PSII X-ray structure at 1.9 Å resolution of Umena and co-workers (PDB ID: 3ARC)[6] as the search model, which was modified by removing waters, detergents, lipids and alternative conformers of the amino acids. We used monomer 1 of the PSII dimer (in which the monomer 1 subunits are labelled with capital letters and small letters are used for monomer 2 in 3ARC model) as the search model for molecular replacement to solve the phase problem by using the program phaser (version 2.5.3). After we found monomer 1, we repeated the search for monomer 2.

Refinement

Both structures were refined by phenix.refine[44] using rigid body refinement, where each C-alpha chain of each protein subunit was considered as a rigid body. The cofactors were also considered as rigid bodies. During the rigid body refinement, we considered only translational refinement and not rotational refinement of the rigid entities. So, the RMS bond angle was not refined. We used the original B factors from the 3ARC model because B-factor refinement is not useful at the given resolution of 5.0 Å. After three refinement cycles, *R*-factors for the dark state at 5.0 Å of R_{work} of 0.260 (R_{free} = 0.262) were observed. The *R*-factors for the double-flash state at 5.5 Å, are R_{work} of 0.280 (R_{free} = 0.290). Refinement statistics are shown in Table 1.

All figures displaying structures were made using PyMOL (DeLano Scientific; http://www.pymol.org).

Calculation of electron density maps

The electron density maps for dark and double-flash data sets were generated using the FFT program from the CCP4 suite. The omit maps, defined by Bhat, were calculated using 'Omit' (CCP4 suite)[45,46] where the OEC was removed from the MR solution. These $(2F_o-F_c)$ omit maps were calculated using experimental data and the MR model excluding the OEC before applying refinement in order to avoid model-bias. For superimposition of these two omit maps from dark and double-flash states respectively, the following steps were carried out. First, using the omit maps as inputs, new sets of coordinate files (PDB files) were generated from the MR solutions of dark and double-flash states separately, so that each of the two omit maps fits the model, using the Molrep program in CCP4 suite. Second, the modified coordinate files for the dark and double-flash states, outputs of Molrep program, were opened, and the superimposed coordinates were saved in the Coot program[47].

The double-flash state coordinate file was considered as the moving object and the dark state coordinate file as the fixed object. As a result, Coot provided Euler angles and translational coordinates (*x*, *y*, *z* values) for this superposition. Third, using these Euler angles and translational coordinates as rotational operator with opposite sign, the double-flash state omit map was rotated using the MAPMASK program in the CCP4 suite. Because the unit cell constants of the dark and double-flash electron density maps differ, they are in different frames of inertia, which we have to take into account for the overlaying process. The rotated double-flash state omit map (output of MAPMASK program) was moved over the superimposed coordinate file. The same procedure was applied to the dark state omit map aligning with the superimposed double-flash coordinate file using MAPMASK program in the CCP4 suite. Examples of the electron density maps are shown in Extended Data Figs 5–7.

Calculation of simulated annealed omit maps

The solutions from the molecular replacement for the PSII dimer for the dark and double-flash states were used for the calculation of the simulated annealed (SA) omit maps[48]. For each of the PSII coordinate files of the MR solutions, the OEC was removed and then the resulting PSII coordinate file was used for calculating the SA-omit map with a starting temperature of 5000 K using the 'AutoBuild create omit map' program from the Phenix suite (version 1301 dev)[49]. The SA omit maps of the OEC in the dark state (S_1) and the double-flash (putative S_3) state are shown in Fig. 3a, b and also see Extended Data Fig. 8 for the dark state SA omit map from a different viewpoint.

Unit cell increase

The conformational change and associated unit cell changes may be caused by dissociation of the mobile plastoquinone PQ_B from the Q_B binding pocket after double-flash excitation, when PSII may reach the S_3 state (see Fig. 1a). The structural changes leading to the difference in unit cell constants are probably most significant at the stromal side of PSII where the quinone bindings sites are located. To avoid structural heterogeneity at the acceptor side by partial re-occupation of the Q_B binding site, no quinone was added to the crystals for the double pump experiments. We thereby may have 'trapped' PSII in the double flash experiment in the putative S_3 state conformation with an empty Q_B binding pocket. In order to transition from S_3 to S_4, an electron acceptor must replenish the empty Q_B binding site. Therefore, the plastoquinone derivative PQ_{decyl}, which diffuses into the Q_B pocket, was added to the crystals used for the triple-flash excitation data set. With the Q_B binding site re-occupied, the change in unit cell constants is reversed.

Structural changes of the OEC

In light of new results on theoretical modelling of the OEC[3,4,18,21,22,50], we further examined the SA-omit maps in the dark and double-flash states for differences in the metal cluster that can be detected even at low resolution and discuss the results here in light of recent computational and spectroscopic studies on the metal cluster. The changes in the density of the Mn_4CaO_5 metal cluster are suggestive of an increase of the distance between the cubane and the 'dangler' Mn and a distortion of the cubane in the S_3 state. The observed electron densities are compared in Fig. 3a and 3b with the recent theoretical studies of Isobe

and co-workers[4], shown in Fig. 3d, who predicted a 'breakage' of the dangler Mn from the cubane cluster in the S_3 state. Additionally, EXAFS data constrains the extent of the movement of the dangler Mn relative to the cubane[51,52]. The increase in distance could allow for the binding of the second substrate water molecule between the dangler Mn and the Mn_3CaO_x cubane. The presence of a substrate water molecule between the dangler Mn and the distorted cubane in the higher S-states, has also been predicted to be essential for the catalytic mechanism in a recent DFT model of the full catalytic S-state cycle, including modelling of the substrate water exchange[21,53]. In addition to the elongation, the overall dimensions of the Mn_4CaO_5 cluster appear to condense in the double-flash data set that may represent the putative S_3-state. This may include shrinking of the distance between the Ca^{2+} and the 3 Mn in the distorted cubane. EXAFS studies on PSII, where the Ca was substituted with Sr, showed significant changes in Mn–Mn or Mn–Sr distances in the S_3 state[24], which were interpreted to indicate the distance between Mn and Ca would shrink in the S_3 state. Our experimental findings suggest a shrinking of the Mn_4CaO_5 cluster in double-flash state, which supports the hypothesis of a condensation of the Mn_3O_xCa cubane part of the Mn_4CaO_5 cluster in S_3 (ref. 4). Models of Mn–oxygencubane compounds show an increased distance between the Mn and O atoms in the cubane at lower oxidation states (+2 and +3) because of the Jahn-Teller (JT) effect[22,54]. Distances derived from a recently published model Mn–O and Mn_3O_xCa cubane structures[55] indicate that Mn–O distances depend on the oxidation states of the Mn-ions: the average Mn^{+2}–O distance is 2.2 Å, the average Mn^{+3}–O distance is 2.0 Å and the average Mn^{4+}–O distance is 1.8 Å. Two models have been proposed on the basis of X-ray absorption and emission spectroscopy, one describes the S_3 state as Mn (+3 +4 +4 +4) and the other proposes Mn (+4 +4 +4 +4)[25,56]. In the model in which all Mn ions have reached the Mn^{+4} oxidation state, a significant shrinking of the dimension of the cluster is expected due to the lack of the JT distortion with the average Mn–O distance being reduced to 1.8 Å (ref. 54). The shrinking of the overall dimensions of the metal cluster, supported by our maps of the double-flash state, appears to be in agreement with the studies on model compounds. This indicates that the JT distortion diminishes in the putative S_3 state during progression of the S-states cycle when all Mn reach their +4 oxidation states[55].

The SA-omit maps of the dark (S_1) and the double-flash (putative S_3) states may be also indicative of changes in the protein environment of the Mn_4CaO_5 cluster. Although the electron density map in the dark S_1 state overall follows the protein backbone of the 1.9 Å structure, larger perturbations of the protein environment of the cluster are visible in the double-flash state. The double-flash state electron density map may suggest a movement of the loop which connects the transmembrane helices C and D (that is, the CD loop) at the lumenal side which includes D170, away from the metal cluster and a movement of the AB loop (connecting the transmembrane helices A and B) into closer vicinity to the cluster, which may allow D61 to become part of the ligand sphere of the metal cluster. Although this interpretation of changes in the protein environment of the cluster is highly speculative at the given resolution, it could explain the results of mutagenesis studies on PSII. Although the mutation of D170A (which coordinates the dangler Mn and the Ca in the 1.9 Å structure of PSII) has no strong effects on the oxygen evolution function[23,57], less than 15% of the oxygen evolution function remains in the D61A mutation[58,59]. This mutagenesis result was

difficult to rationalize because D61 is found only in the second ligand sphere of the OEC in the 1.9 Å structure[6]. However, our SA-Omit electron density map of the metal cluster in the double-flash state shows a connection to the protein electron density in close vicinity toD61 (see Fig. 3b). This finding may provide a first indication that D61 may serve as a ligand to the dangler manganese in the higher S-states. Although details of the conformational changes cannot be unravelled at the current resolution of 5 Å, the comparison of the dark and double-flash state SA omit maps provide an indication that the protein ligand sphere of the Mn_4CaO_5 cluster may undergo significant changes when the OEC reaches the double-flash (putative S_3) state.

Extended Data

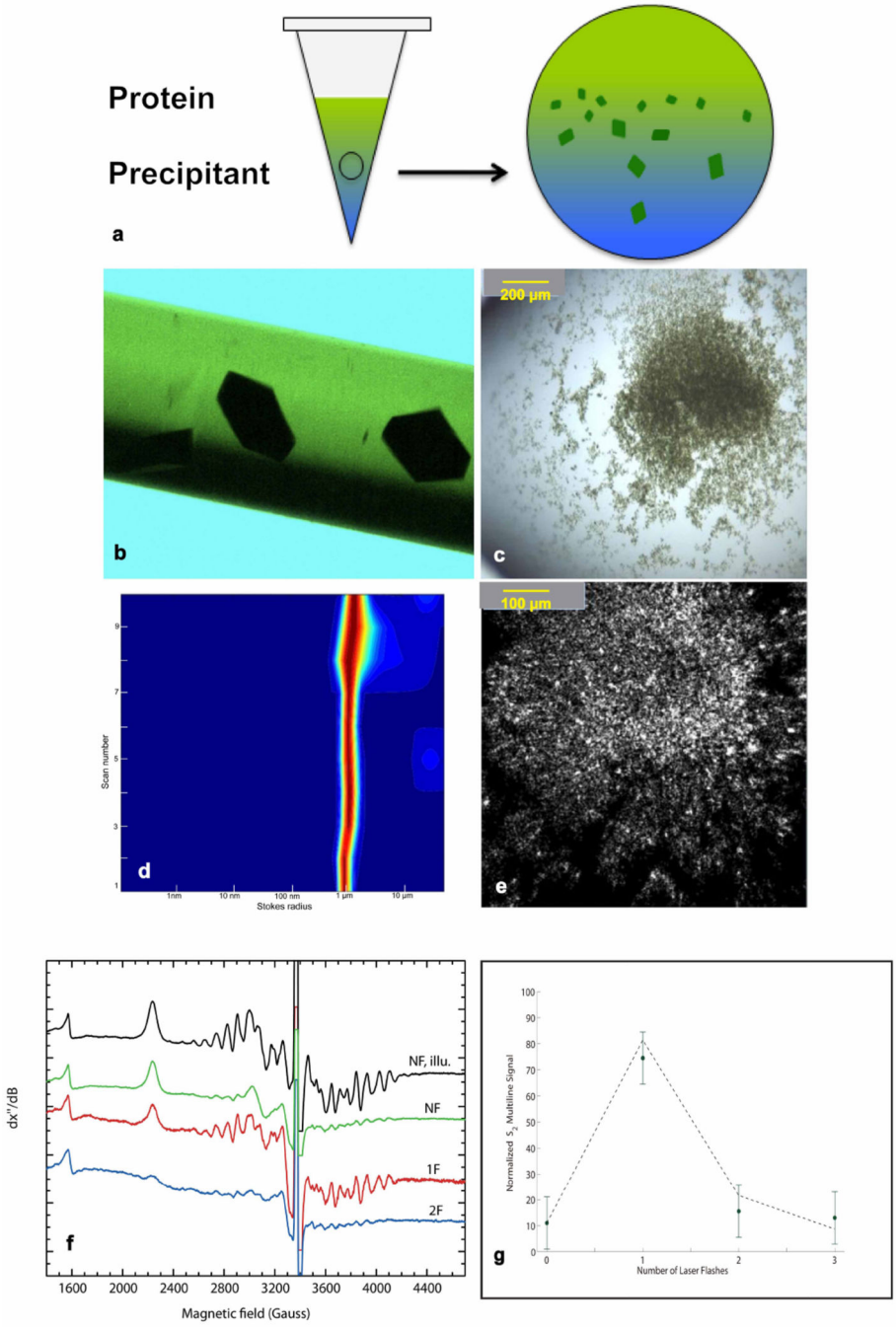

Extended Data Figure 1. Photosystem II crystal growth and characterization

a, Scheme of free interface diffusion enhanced sedimentation method for growth of photosystem II nano/microcrystals. **b**, Large photosystem II crystals (average size 300 µm) suitable for X-ray data collection at synchrotron sources. **c**, Optical image of nano/microcrystals of photosystem II grown by free interface diffusion used for the TR-SFX data collection at LCLS. The crystallinity must be confirmed by other methods such as SONICC

(see (**e**) for the SONICC image of the crystals) because nanocrystals look similar to amorphous precipitate. **d**, DLS results of the crystals shown in **c** indicate an average Stokes radius of 1 μm. **e**, SONICC image of the photosystem II microcrystals shown in **c**. **f**, **g**, Panels showing the EPR analysis of S-states yield of PSII after double-excitation. **f**, X-band EPR spectra (10 K) of photosystem II protein solution used for crystallization exposed to 0 (dark adapted sample, no flash NF), one (1F) or two (2F) saturating laser excitation flashes at room temperature. The samples were flash frozen after illumination. For comparison we also show the EPR spectra of dark adapted photosystem II subjected to continuous illumination at 190 K (NF, illu). At low temperature, the S-state cycle stops in the S_2 state which means that this conditions corresponds to the maximal yield of multi-line signal. Three individual samples of each type were analysed and the same MLS intensities were consistently found for similar samples. **g**, Fit of the quantified S_2 state multiline signal (MLS) oscillations to the Kok model of the S-state transition cycle[31]. Please note that the MLS yield after the second and third flash is nearly constant in the measurements, whereas the fit predicts a decline after the third flash. This is expected as we have not added quinones or artificial electron acceptors to the sample, so that there is no terminal electron acceptor present after PQH_2 has left the Q_B binding site after the second flash.

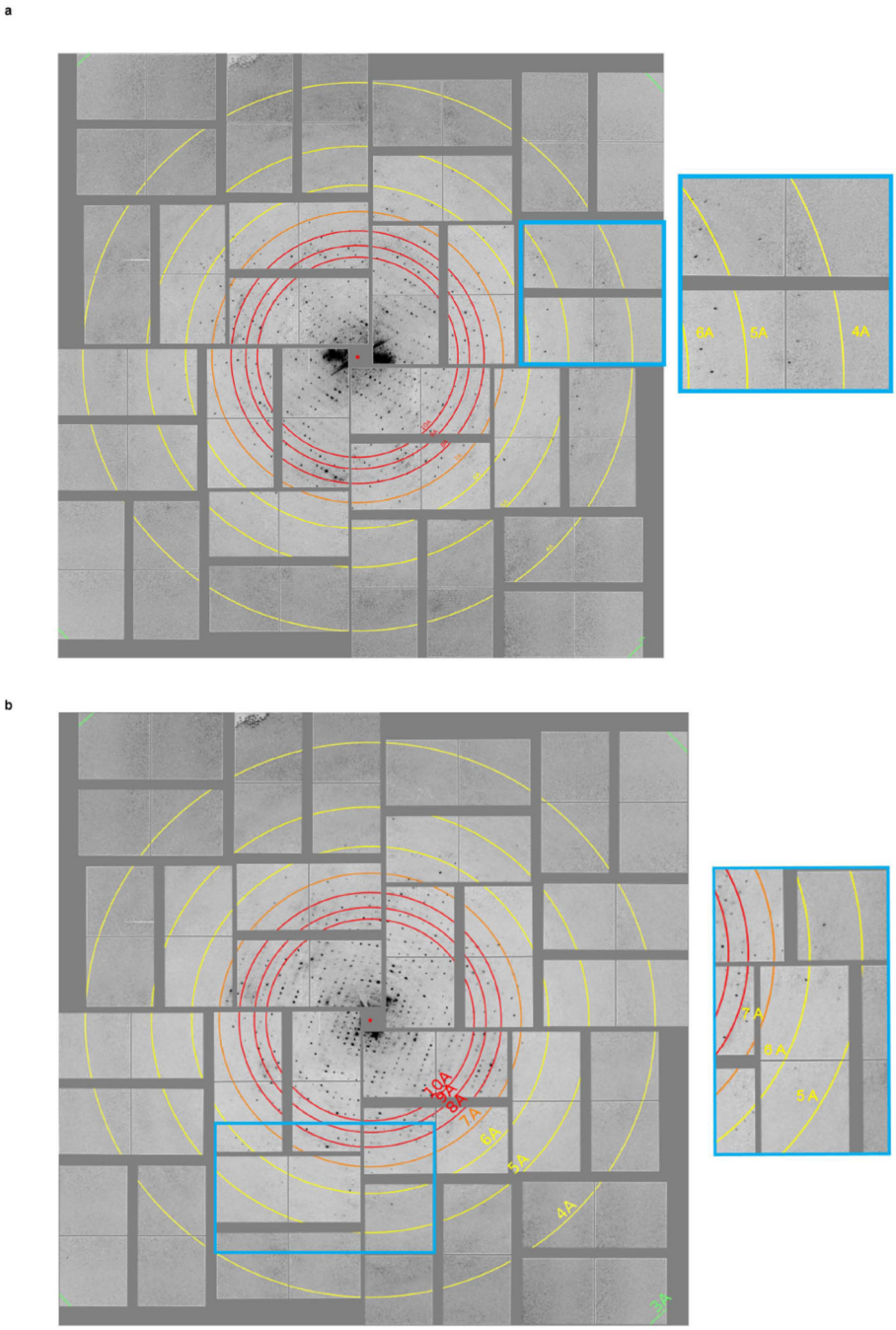

Extended Data Figure 2. Background corrected diffraction pattern of a photosystem II microcrystal

a, **b**, From the dark (S_1) data set (**a**) and the double-flash data set (**b**) collected at the CXI instrument at LCLS. The resolution is indicated by red and yellow rings corresponding to resolution shells in Å 10, 9, 8 (red), 7 (orange), 6, 5, 4 (yellow). The right panel shows an enlarged view of the diffraction patterns (see blue box).

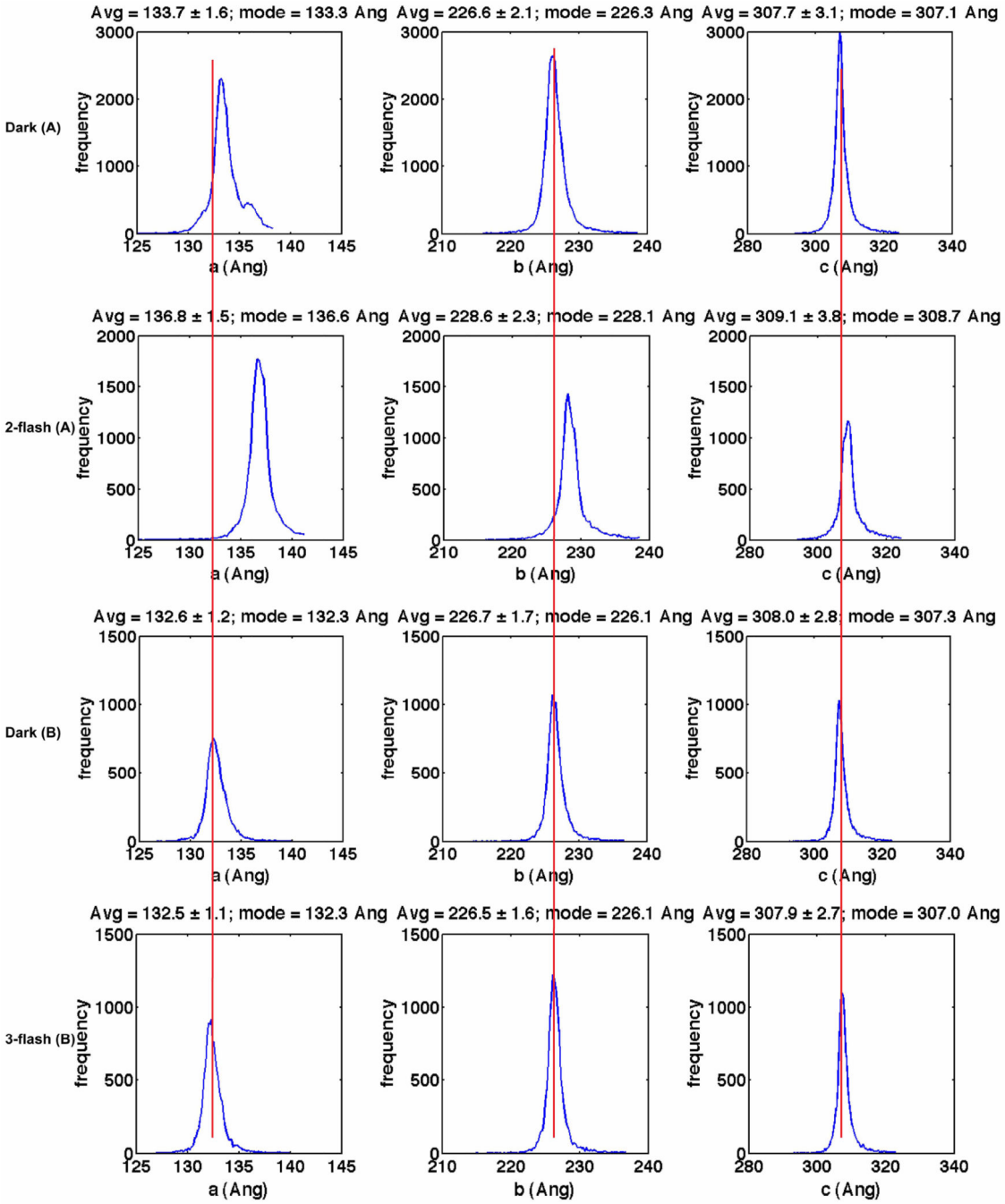

Extended Data Figure 3. Distribution of photosystem II unit cell constants of 4 different femtosecond crystallography data sets

Row 1 (top row) shows unit cell constants of the dark data set (S_1 state) collected at the CXI instrument in January 2012 (experiment (A)). Row 2 shows unit cell constants of the double-flash data set (putative S_3 state) collected at the CXI instrument in January 2012 (experiment (A)). Row 3 shows unit cell constants of the dark data set (S_1 state) collected at the CXI instrument in June 2012 (experiment (B)) (quinone PQ_{decyl} was added to these crystals to allow replacement of the quinone for triple excitation). Row4 shows unit cell constants of the triple-flash data set (putative S_4 state) collected at the CXI instrument in June 2012

(experiment (B)). The comparison of unit cell constants shows that significant changes in the unit cell constants are observed after double-flash excitation of photosystem II. These changes are fully reversed when photosystem II is excited by three laser flashes. Although the number of indexed patterns currently available does not yet allow for the determination of an accurate structure of the PSII after triple excitation, the data allows extraction of information on the hit rates, indexing rates and unit cell constants, showing that the unit cell constants are identical for the dark S_1 and triple-flash state.

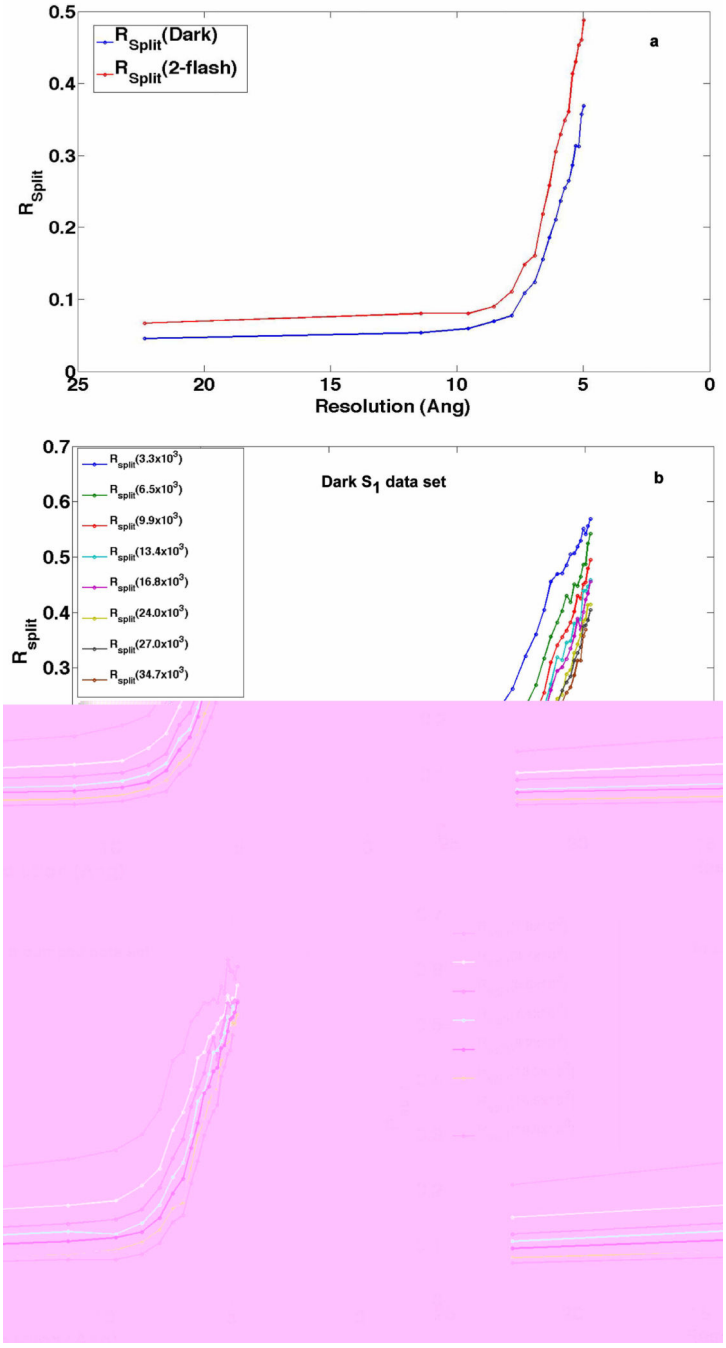

Extended Data Figure 4. R_{split} as a function of resolution bins and number of indexed patterns

a, R_{split} as a function of the resolution shell (in total 20 bins) for dark state data (blue) and double-pumped state data (red). **b**, R_{split} as a function of resolution bins for dark S_1 state, R_{split} decreases indicating better data quality with increase in number of indexed patterns from 3,300 to 34,000 images. **c**, R_{split} as a function of resolution bins for the dark and double-flash states, the R_{split} decreases indicating better quality with increase in number of indexed patterns from 1,800 to 18,800 images.

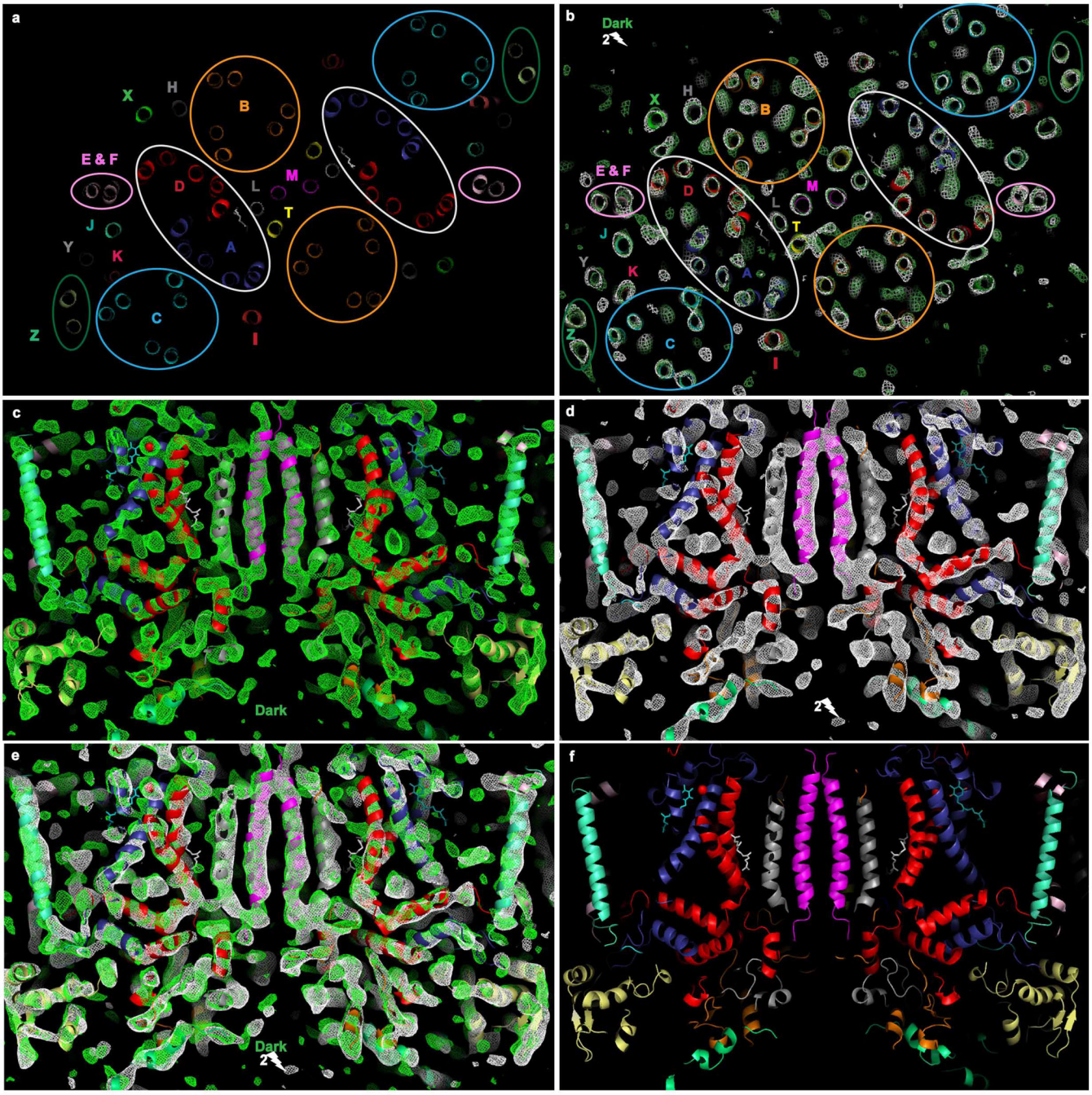

Extended Data Figure 5. The arrangement of the transmembrane helices in the photosystem II dimer

a, **b**, An overview of the arrangement of transmembrane helices in photosystem II. The protein subunits are named according to their genes so PsbA is subunit A, PsbB is subunit B, etc. The identification of the location of subunits with more than one transmembrane helix is facilitated by ovals, which are labelled using the same colour code as the corresponding subunit. **a**, Top view from the stromal side of the arrangement of transmembrane helices in the middle of the membrane. The assignment of helices to different protein subunits is based on the structural assignments of ref. 6. The 5 transmembrane helices of the core subunits of the reaction centre are PsbA (blue) and PsbB (red). **b**, The picture shows the omit maps ($2F_o-F_c$) of the dark and double-flash states at the contour level of 1.5 σ in the same view direction as shown in Extended Data Fig. 5a. **c**–**f**, These panels show that most of the alpha helices in the middle of the membrane are well matched between the dark and double-flash states, in the reaction centre core (PsbA and PsbB) as well as in the peripheral parts of photosystem II (for example PsbZ). The view and colour coding of helices are the same as in Extended Data Fig. 5a. **c**, **d**, Omit maps of the dark (green) and double-flash (white) states of PSII show a cut through the central region of photosystem II at 1.5 σ. **e**, The superposition of omit maps indicates a good general overlay of the transmembrane helices and the lumenal loop regions in the two omit maps featuring the reaction centre core subunits PsbA (blue) and PsbB (red) as well as the peripheral subunit X (cyan), and the subunits M(pink) and L (grey) in the dimerization domain of the photosystem II dimer. The electron density is shown at the contour level of 1.5 σ. **f**, The structural model is also shown with same colour codes as in Extended Data Fig. 5a.

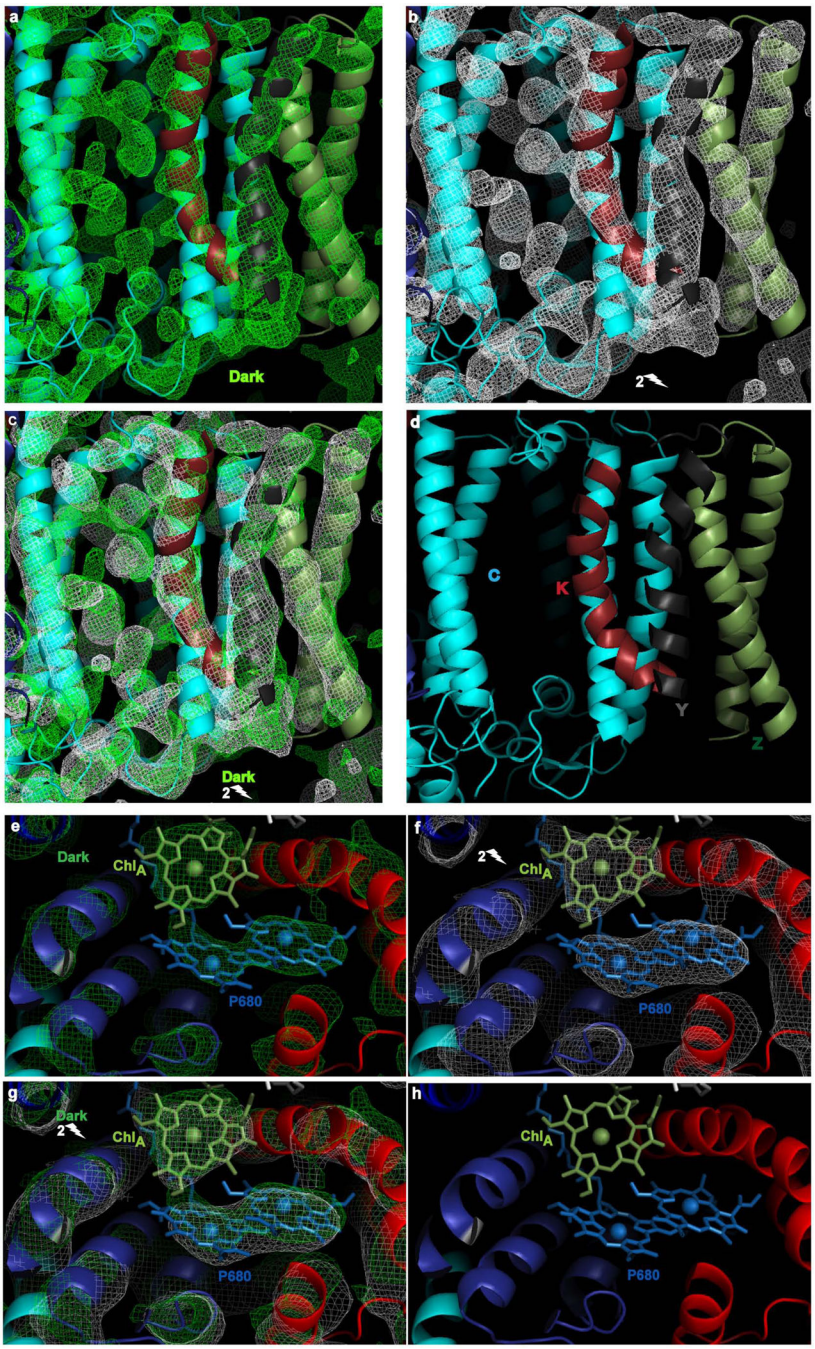

Extended Data Figure 6. Omit map of the dark and double-flash states of the most peripheral photosystem II membrane integral subunits and the chlorophylls of the primary electron donor P680

a–**d**, This picture features the peripheral subunits PsbZ (grey-green), PsbK (brown), PsaY (grey) and the core-antenna protein CP43 (PsbC) (cyan). The omit electron density map at the contour level of 1.5 σ for the dark (S_1) state is depicted in green (**a**) and the double-flash (putative S_3) state is depicted in white (**b**). **c**, The overlay of the two omit maps is shown at the contour level of 1.5 σ. The globular densities between PsbC and PsbK correspond to antenna chlorophylls. The figure shows that even the electron density for the two most

peripheral helices that belong to subunit PsbZ are well defined. We also note the good match of the strongly kinked helix of PsbK between the S_1 and S_3-state electron density maps. **d**, The subunits are labelled according to their genes in the view of the structural model. **e**–**h**, The figure features the surroundings of the two chlorophylls of P680 and the accessory chlorophyll of the active electron transfer branch of photosystem II (see Fig. 2c). The omit electron density map at the contour level of 1.5 σ for the dark (S_1) state is depicted in green (**e**) and the double-flash (putative S_3) state is depicted in white (**f**). **g**, The figure also shows the overlay of the two omit maps at the contour level of 1.5 σ. **h**, Model of the chlorophylls of the primary electron donor P680 without electron density map.

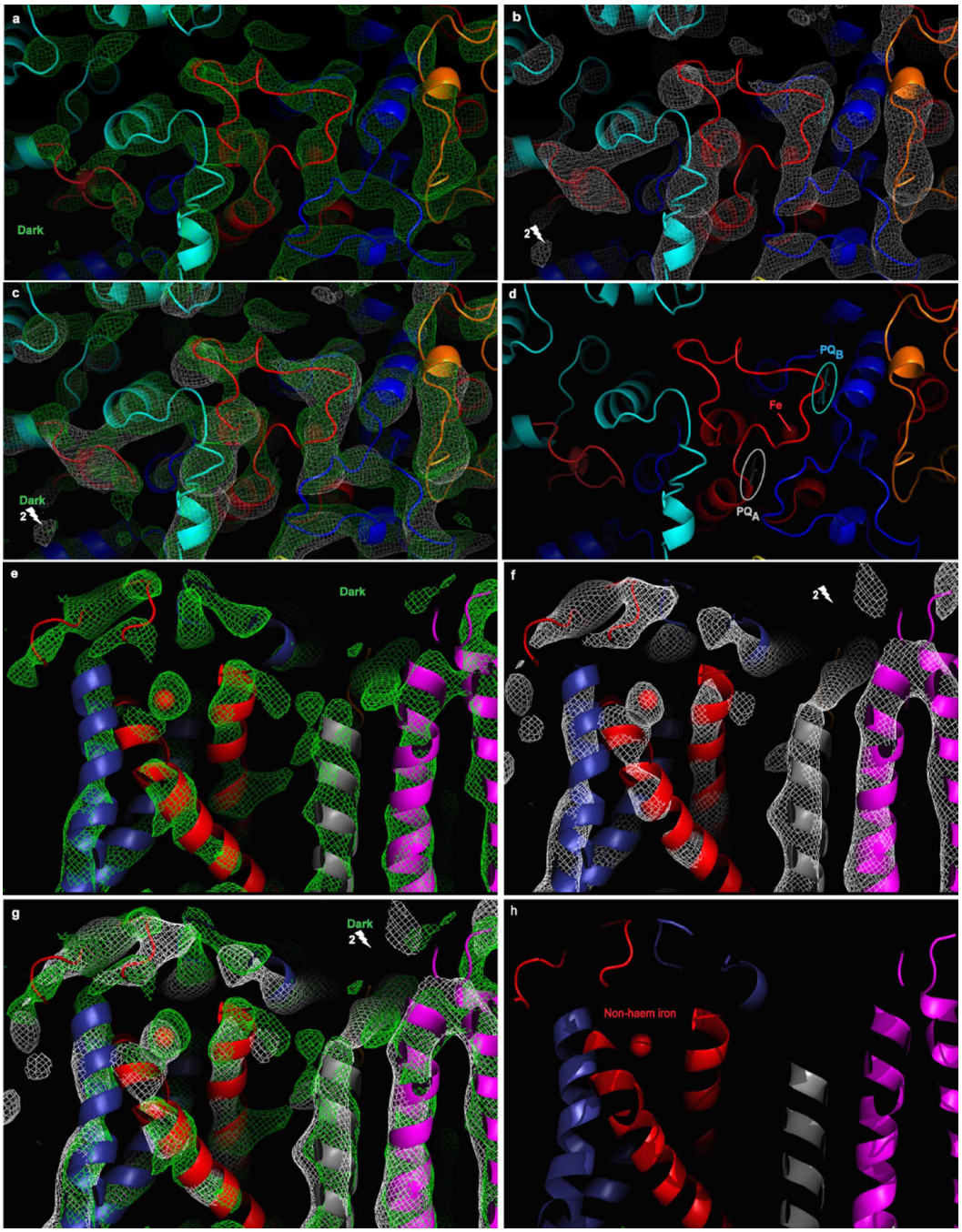

Extended Data Figure 7. The electron acceptor side of photosystem II

Omit map electron density and structural model of the dark and double-flash state of photosystem II, the view from the stromal side onto the membrane plane. **a**–**d**, The loops that coordinate the non-haem iron and cover the quinone binding sites looking from the stromal side onto the membrane plane. The omit electron density map at the contour level of 1.5 σ for the dark (S_1) state is depicted in green (**a**) and the double-flash (putative S_3) state is depicted in white (**b**). **c**, The overlay of the two omit maps at 1.5 σ. **d**, The structural model indicates the positions of PQ_A and PQ_B as well as the non-haem iron located below the

loops. We note that the electron densities of the loop regions at the electron acceptor side show significant differences between the dark and the double-flash states. The electron density of both states may suggest a conformation of the loops that could differ in their backbone trace from the model derived from the 1.9 Å structure from ref. 6. **e**–**h**, The side view of the acceptor side of photosystem II along the plane in the membrane. The omit electron density map at the contour level of 1.5 σ for the dark (S_1) state is depicted in green (**e**) and the double-flash (putative S_3) state is depicted in white (**f**). **g**, The overlay of the two omit maps featuring the changes in the position of the non-haem iron and loop regions at the contour level of 1.5 σ. **h**, Model of the electron acceptor side of photosystem II. The protein subunits are colour coded as in Extended Data Fig. 5a of the main text; the non-haem iron is depicted as a red sphere. The tightly bound plastoquinone PQ_A is shown in white, the mobile plastoquinone PQ_B is depicted in cyan.

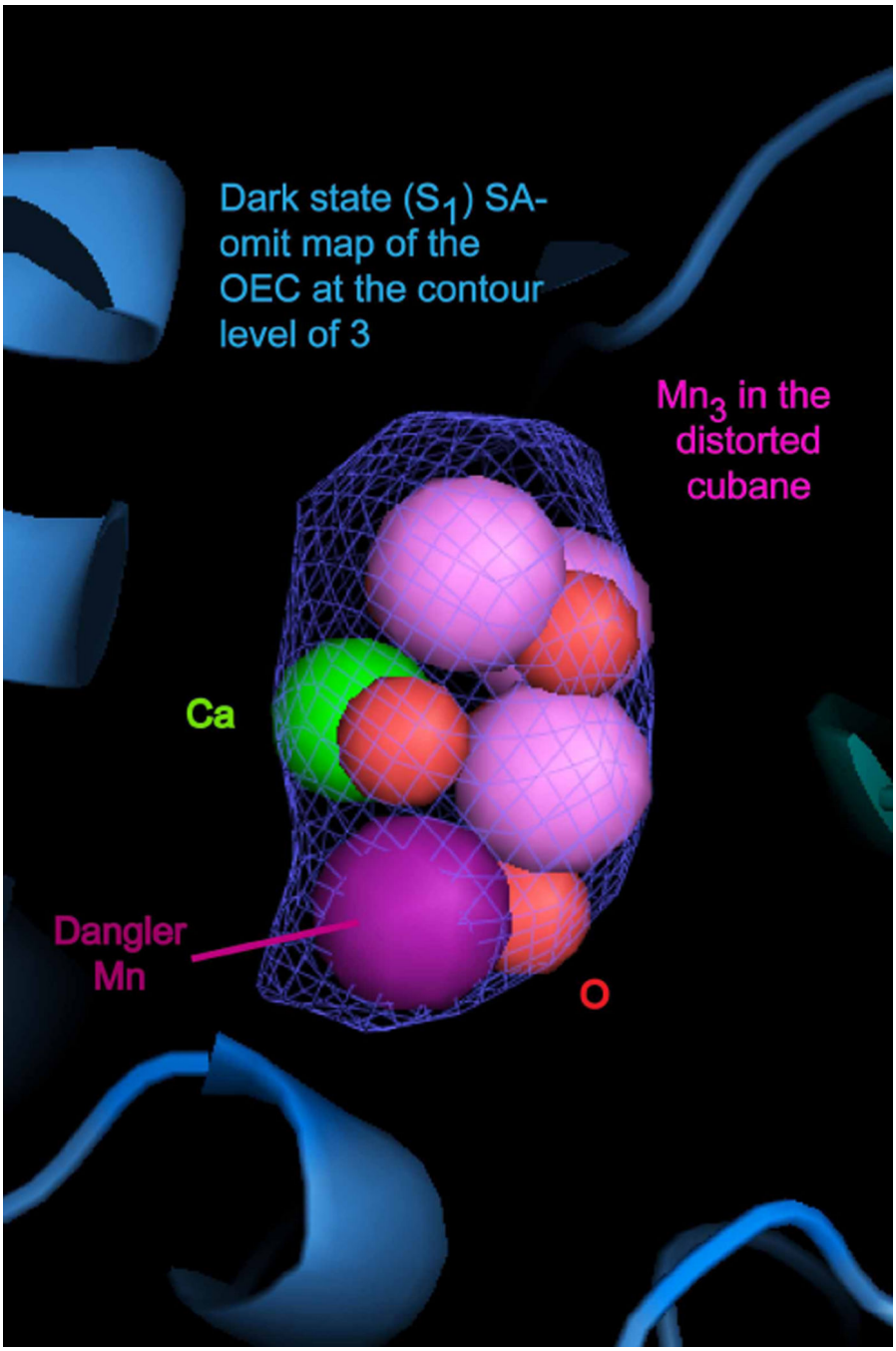

Extended Data Figure 8. Simulated annealed omit map of the Mn_4CaO_5 cluster of photosystem II

The electron density of the dark state of photosystem II. This figure shows the superimposed SA-omit maps for the dark (S_1) (blue) state of the Mn_4CaO_5 cluster. We use a different colour scheme for the SA-omit maps and the 'regular $2F_o-F_c$' omits maps to allow the reader a better orientation of the type of map shown in each figure. The electron density is shown at the contour level of 3.0 σ to ensure that it solely features the metal Mn_4CaO_5 cluster. The X-ray structure at 1.9 Å from ref. 6 is placed inside the SA-omit map for comparison. The nomenclature for the Mn atoms proposed in ref. 6 is used for the colour-

coding of the individual Mn atoms in the cluster. The Mn ions that form the distorted Mn_3O_xCa cubane (Mn1, Mn2 and Mn3) are depicted in light pink, while Mn4 (violet) (referred to as the dangler Mn) is located outside the cubane. This figure shows that the dangler Mn sticks out of the SA-omit map electron density, which indicates that this Mn atom may be located in closer proximity to the Mn_3O_xCa cubane in the dark S_1 state that is not influenced by X-ray damage.

Extended Data Table 1

Statistics of the femtosecond crystallography X-ray diffraction data sets

a

Resolution (Å)	observed unique reflections	Measurements	Completeness (%)	Multiplicity	I/σ(I)	$CC_{1/2}$	Reflections (used for $CC_{1/2}$)
19.20	4,255	3,081,618	99.63	724.2	23.12	0.990	4,236
9.60	4,038	3,048,418	99.48	754.9	16.69	0.991	4,017
8.03	3,980	3,064,098	99.20	769.9	12.26	0.989	3,926
7.17	3,928	2,847,009	98.35	724.8	8.04	0.977	3,783
6.58	3,826	2,608,679	96.28	681.8	5.67	0.957	3,552
6.16	3,808	2,497,532	95.70	655.9	4.31	0.936	3,446
5.82	3,682	2,552,117	92.91	693.1	3.59	0.903	3,200
5.55	3,663	2,548,799	92.73	695.8	3.21	0.890	3,105
5.32	3,543	2,489,203	90.04	702.6	2.75	0.853	2,822
5.13	3,426	2,241,076	86.95	654.1	2.41	0.826	2,664
4.96	3,555	2,193,921	90.46	617.1	2.29	0.740	2,767
4.81	3,518	2,241,551	89.84	637.2	2.10	0.695	2,655
4.68	3,448	2,246,609	88.23	651.6	1.89	0.392	2,549
4.56	3,439	2,201,217	86.95	640.1	1.77	0.463	2,422
4.45	3,316	2,176,673	84.85	656.4	1.69	0.445	2,327
4.36	3,166	2,097,792	81.87	662.6	1.52	0.216	2,078
4.27	3,116	2,116,675	78.86	677.7	1.47	0.135	1,963
4.18	2,995	2,097,219	77.03	700.2	1.40	0.070	1,841
4.11	2,850	2,009,233	73.00	705.0	1.27	0.062	1,607
4.03	2,930	2,032,330	74.99	693.6	1.32	0.068	1,721
Overall	**70,482**	**48,386,769**	**88.85**	**684.93**	**5.42**	**0.994**	**56,691**

b

Resolution (Å)	observed unique reflections	Measurements	Completeness (%)	Multiplicity	I/σ(I)	$CC_{1/2}$	Reflections (used for $CC_{1/2}$)
19.20	4,395	1,724,037	99.30	392.3	16.30	0.974	4,361
9.60	4,157	1,728,443	98.79	415.8	11.84	0.983	4,103
8.03	4,085	1,718,604	97.80	420.7	8.71	0.977	3,960
7.17	3,916	1,546,207	94.73	394.8	5.72	0.963	3,628
6.58	3,747	1,389,049	90.73	370.7	3.93	0.926	3,242

b

Resolution (Å)	observed unique reflections	Measurements	Completeness (%)	Multiplicity	I/σ(I)	$CC_{1/2}$	Reflections (used for $CC_{1/2}$)
6.16	3,671	1,308,516	88.97	356.4	2.91	0.860	3.001
5.82	3,463	1,306,601	84.28	377.3	2.35	0.789	2,626
5.55	3,365	1,280,059	82.27	380.4	2.06	0.785	2,439
5.32	3,193	1,221,532	77.90	382.6	1.79	0.635	2,202
5.13	2,946	1,046,614	72.05	355.3	1.60	0.474	1,893
4.96	3,107	1,040,022	76.28	334.7	1.51	0.450	1,935
4.81	3,046	1,056,445	74.84	346.8	1.45	0.308	1,847
4.68	3,078	1,087,015	75.20	353.2	1.40	0.167	1,890
4.56	2,968	1,034,930	73.16	348.7	1.34	0.159	1,764
4.45	2,859	1,021,562	70.26	357.3	1.30	0.086	1,649
4.36	2,771	1,003,272	68.20	362.1	1.22	0.007	1,510
4.27	2,652	979,252	65.37	369.3	1.17	0.042	1,394
4.18	2,628	1,001,005	65.15	380.9	1.18	0.072	1,386
4.11	2,447	937,143	59.95	383.0	1.13	0.010	1,294
4.03	2,579	976,398	64.00	378.6	1.14	0.037	1,350
Overall	**65,073**	**24,496,706**	**78.96**	**373.04**	**4.09**	**0.988**	**47,474**

Statistics of the femtosecond crystallography X-ray diffraction data set of **a**, the dark (S_1) state by resolution bins**, and **b**, the double-flash (putative S_3) state by resolution bins.

** $CC_{1/2}$ is Peasrson's coefficient calculted as described in ref. 29.

Extended Data Table 2

Data statistic comparison of hit and indexing rates as well as the unit cell constants from 4 different data sets collected on photosystem II crystals

a

	Dark (A)	2-flash(A)	Dark (B)	3-flash(B)
Crystal hits	71,628	63,363	33,373	32,190
Indexed images	34,554	18,772	11,664	12,543
Indexing rate (%)	48	29	35	38
Unit cell constant a (Å)	133.3 ± 1.6	136.6 ± 1.5	132.3 ± 1.2	132.3 ± 1.1
Unit cell constant b (Å)	226.3 ± 2.1	228.1 ± 2.3	226.1 ± 1.7	226.1 ± 1.6
Unit cell constant c (Å)	307.1 ± 3.1	308.7 ± 3.8	307.3 ± 2.8	307.0 ± 2.7

b

	Dark (A) (only dark)	Dark (A) (dark alternating with illumination)
Crystal hits	12,087	59,541
Indexed images	5,170	29,384
Indexing rate (%)	42.77	49.35

b

	Dark (A) (only dark)	Dark (A) (dark alternating with illumination)
Unit cell constant a (Å)	133.2 ± 1.9	133.3 ± 1.5
Unit cell constant b (Å)	225.8 ± 2.2	226.3 ± 2.0
Unit cell constant c (Å)	307.6 ± 3.2	307.1 ± 3.1

c

	Kern et. al (2013)		This work	
	S_1	S_2	Dark (S_1)	2-flash (putative S_3)
Resolution range (Å)	82.9 – 5.7 (5.9 – 5.7)	83.0 – 5.9 (6.1 – 5.9)	100.6 – 5.0 (5.11 – 5.0)	102.3 – 5.5 (5.66 – 5.5)
Total reflection	1,475,630 (8,036)	564,722 (8,662)	28,679,554 (1,679,683)	12,476,013 (1,018,721)
Unique reflections	27,220 (2,290)	24,671 (2,143)	40,946 (2,710)	32,066 (2,651)
Multiplicity	54.2 (3.5)	22.9 (4.0)	700.35 (618.0)	388.55 (381.1)
$CC_{1/2}$	0.802 (0.343)	0.661 (0.376)	0.914 (0.740)	0.877 (0.635)
R_{work}	0.276 (0.360)	0.284 (0.306)	0.260 (0.350)	0.280 (0.382)
R_{free}	0.315 (0.350)	0.317 (0.387)	0.262 (0.343)	0.290 (0.347)

a, The data sets dark (A) and double-flash (A) were collected at the CXI instrument in January 2012 and may represent the dark S_1 state and putative S_3 state of photosystem II for which data evaluation and structural changes are discussed in this work. For comparison, the statistics are shown for data sets collected on the dark state S_1 and the transient triple-flash state (that is, putative S_4 state) at the CXI instrument in June 2012. **b**, Data statistics for dark (A) separated into runs where the laser was switched off (only dark state) and dark state images from runs where alternate dark and light states patterns were recorded. **c**, Data statistics from this work and from Kern *et al.* (2013) (ref. 13). Comparison of the data evaluation statistics of the dark S_1 state and double-flash (putative S_3) state data from this work evaluated by the CrystFEL software suite[17] along with data from ref. 13 on the dark S_1 state and the single excited S_2 state evaluated with the software suite cctbx.xfel[30]. The numbers in brackets refer to the data statistics in the highest resolution shell.

Authors

Christopher Kupitz[1,*], Shibom Basu[1,*], Ingo Grotjohann[1], Raimund Fromme[1], Nadia A. Zatsepin[2], Kimberly N. Rendek[1], Mark S. Hunter[1,3], Robert L. Shoeman[4], Thomas A. White[5], Dingjie Wang[2], Daniel James[2], Jay-How Yang[1], Danielle E. Cobb[1], Brenda Reeder[1], Raymond G. Sierra[6], Haiguang Liu[2], Anton Barty[5], Andrew L. Aquila[5,7], Daniel Deponte[5,8], Richard A. Kirian[2,5], Sadia Bari[9,10], Jesse J. Bergkamp[1], Kenneth R. Beyerlein[5], Michael J. Bogan[6], Carl Caleman[5,11], Tzu-Chiao Chao[1,12], Chelsie E. Conrad[1], Katherine M. Davis[13], Holger Fleckenstein[5], Lorenzo Galli[5,14], Stefan P. Hau-Riege[3], Stephan Kassemeyer[4,9], Hartawan Laksmono[6], Mengning Liang[5], Lukas Lomb[4], Stefano Marchesini[15], Andrew V. Martin[5,16], Marc Messerschmidt[8], Despina Milathianaki[8], Karol Nass[4,5,14], Alexandra Ros[1], Shatabdi Roy-Chowdhury[1], Kevin Schmidt[2], Marvin Seibert[8,17], Jan Steinbrener[4], Francesco Stellato[5], Lifen Yan[13], Chunhong Yoon[5,7], Thomas A.

Moore[1], Ana L. Moore[1], Yulia Pushkar[13], Garth J. Williams[8], Sébastien Boutet[8], R. Bruce Doak[2], Uwe Weierstall[2], Matthias Frank[3], Henry N. Chapman[5,14,18], John C. H. Spence[2], and Petra Fromme[1]

Affiliations

[1]Department of Chemistry and Biochemistry, Arizona State University, Tempe, Arizona 85287-1604, USA

[2]Department of Physics, Arizona State University, Tempe, Arizona 85287, USA

[3]Lawrence Livermore National Laboratory, Livermore, California 94550, USA

[4]Max-Planck-Institut für medizinische Forschung, Jahnstrasse 29, 69120 Heidelberg, Germany

[5]Center for Free-Electron Laser Science, DESY, Notkestrasse 85, 22607 Hamburg, Germany

[6]Stanford PULSE Institute, SLAC National Accelerator Laboratory, 2575 Sand Hill Road, Menlo Park, California 94025, USA

[7]European XFEL GmbH, Notkestrasse 85, 22607 Hamburg, Germany

[8]Linac Coherent Light Source, Stanford Linear Accelerator Center (SLAC) National Accelerator Laboratory, 2575 Sand Hill Road, Menlo Park, California 94025, USA

[9]Max Planck Advanced Study Group, Center for Free-Electron Laser Science (CFEL), Notkestrasse 85, 22607 Hamburg, Germany

[10]Max-Planck-Institut für Kernphysik, Saupfercheckweg 1, 69117 Heidelberg, Germany

[11]Department of Physics and Astronomy, Uppsala University, Regementsvägen 1, SE-752 37 Uppsala, Sweden

[12]University of Regina, 3737 Wascana Pkwy Regina, Saskatchewan S4S 0A2, Canada

[13]Department of Physics, Purdue University, 525 Northwestern Avenue, West Lafayette, Indiana 47907, USA

[14]University of Hamburg, Luruper Chaussee 149, 22761 Hamburg, Germany

[15]Lawrence Berkeley National Laboratory, Berkeley, California 94720, USA

[16]Department ARC Centre of Excellence for Coherent X-ray Science, Department of Physics, University of Melbourne, Parkville VIC 3010, Australia

[17]Uppsala University, Sankt Olofsgatan 10B, 753 12 Uppsala, Sweden

[18]Center for Ultrafast Imaging, Luruper Chaussee 149, 22761 Hamburg, Germany

Acknowledgements

Experiments were carried out at the Linac Coherent Light Source (LCLS), a national user facility operated by Stanford University on behalf of the US Department of Energy (DOE), Office of Basic Energy Sciences (OBES).

This work was supported by the following agencies: the Center for Bio-Inspired Solar Fuel Production, an Energy Frontier Research Center funded by the DOE, Office of Basic Energy Sciences (award DE-SC0001016), the National Institutes of Health (award 1R01GM095583), the US National Science Foundation (award MCB-1021557 and MCB-1120997), the DFG Clusters of Excellence 'Inflammation at Interfaces' (EXC 306) and the 'Center for Ultrafast Imaging'; the Deutsche Forschungsgemeinschaft (DFG); the Max Planck Society, the Atomic, Molecular and Optical Sciences Program; Chemical Sciences Geosciences and Biosciences Division, DOE OBES (M.J.B.) and the SLAC LDRD program (M.J.B., H.L.); the US DOE through Lawrence Livermore National Laboratory under the contract DE-AC52-07NA27344 and supported by the UCOP Lab Fee Program (award no. 118036) and the LLNL LDRD program (12-ERD-031); the Hamburg Ministry of Science and Research and Joachim Herz Stiftung as part of the Hamburg Initiative for Excellence in Research. The research at Purdue University was supported by the U.S. Department of Energy (DOE), Office of Basic Energy Sciences DE-FG02-12ER16340 (Y.P.) and the National Science Foundation Graduate Research Fellowship under Grant 0833366 (K.M.D.). We also want to thank the National Science Foundation for providing funding for the publication of this work through the BioFEL Science Technology Center (award 1231306). We thank H. Isobe, M. Shoji, S. Yamanaka, Y. Umena, K. Kawakami, N. Kamiya, J. R. Shen and K. Yamaguchi for permission to show a section of Fig. 6 of their publication ref. 4 in Fig. 3d of this publication. We thank R. Neutze and his team for support and discussions during joint beamtime for the PSII project and his projects on time-resolved wide-angle scattering studies. We thank A. T. Brunger for discussions concerning data analysis. We thank T. Terwilliger for support with parameter setting of phenix.autobuild program for the SA-omit maps. We also wish to thank R. Burnap for discussions concerning interpretation of results of ligand mutagenesis. We thank J. D. Zook for his contributions concerning plastoquinone quantification. We thank M. Zhu for helping to create high resolution figures for this publication. We thank Raytheon for support of our studies by providing night-vision devices.

References

1. Renger G. Mechanism of light induced water splitting in photosystem II of oxygen evolving photosynthetic organisms. Biochim. Biophys. Acta. 2012; 1817:1164–1176. [PubMed: 22353626]
2. Chapman HN, et al. Femtosecond X-ray protein nanocrystallography. Nature. 2011; 470:73–77. [PubMed: 21293373]
3. Navarro MP, et al. Ammonia binding to the oxygen-evolving complex of photosystem II identifies the solvent-exchangeable oxygen bridge (μ-oxo) of the manganese tetramer. Proc. Natl Acad. Sci. USA. 2013; 110:15561–15566. [PubMed: 24023065]
4. Isobe H, et al. Theoretical illumination of water-inserted structures of the $CaMn_4O_5$ cluster in the S_2 and S_3 states of oxygen-evolving complex of photosystem II: full geometry optimizations by B3LYP hybrid density functional. Dalton Trans. 2012; 41:13727–13740. http://dx.doi.org/10.1039/c2dt31420g. [PubMed: 23037319]
5. Zouni A, et al. Crystal structure of photosystem II from *Synechococcus elongatus* at 3.8 Å resolution. Nature. 2001; 409:739–743. [PubMed: 11217865]
6. Umena Y, Kawakami K, Shen JR, Kamiya N. Crystal structure of oxygen-evolving photosystem II at a resolution of 1.9 Å. Nature. 2011; 473:55–60. [PubMed: 21499260]
7. Boutet S, et al. High-resolution protein structure determination by serial femtosecond crystallography. Science. 2012; 337:362–364. [PubMed: 22653729]
8. Redecke L, et al. Natively inhibited *Trypanosoma brucei* cathepsin B structure determined by using an X-ray laser. Science. 2013; 339:227–230. [PubMed: 23196907]
9. Barty A, et al. Self-terminating diffraction gates femtosecond X-ray nanocrystallography measurements. Nature Photon. 2012; 6:35–40.
10. Aquila A, et al. Time-resolved protein nanocrystallography using an X-ray free-electron laser. Opt. Express. 2012; 20:2706–2716. [PubMed: 22330507]
11. Neutze R, Moffat K. Time-resolved structural studies at synchrotrons and X-ray free electron lasers: opportunities and challenges. Curr. Opin. Struct. Biol. 2012; 22:651–659. [PubMed: 23021004]
12. Spence JCH, Weierstall U, Chapman HN. X-ray lasers for structural and dynamic biology. Rep. Prog. Phys. 2012; 75:102601. [PubMed: 22975810]
13. Kern J, et al. Simultaneous femtosecond X-ray spectroscopy and diffraction of photosystem II at room temperature. Science. 2013; 340:491–495. [PubMed: 23413188]
14. Boutet S, Williams GJ. The coherent X-ray imaging (CXI) instrument at the Linac Coherent Light Source (LCLS). New J. Phys. 2010; 12:035024.

15. Emma P, et al. First lasing and operation of an angstrom-wavelength free-electron laser. Nature Photon. 2010; 4:641–647.
16. Barty A, et al. Cheetah: software for high-throughput reduction and analysis of serial femtosecond X-ray diffraction data. J. Appl. Crystallogr. 2014; 47:1118–1131. [PubMed: 24904246]
17. White TA, et al. CrystFEL: a software suite for snapshot serial crystallography. J. Appl. Crystallogr. 2012; 45:335–341.
18. Luber S, et al. S1-state model of the O_2-evolving complex of photosystem II. Biochemistry. 2011; 50:6308–6311. [PubMed: 21678908]
19. Davis KM, Kosheleva I, Henning RW, Seidler GT, Pushkar Y. Kinetic modeling of the X-ray-induced damage to a metalloprotein. J. Phys. Chem. B. 2013; 117:9161–9169. [PubMed: 23815809]
20. Ames W, et al. Theoretical evaluation of structural models of the S2 state in the oxygen evolving complex of photosystem II: protonation states and magnetic interactions. J. Am. Chem. Soc. 2011; 133:19743–19757. [PubMed: 22092013]
21. Siegbahn PE. Water oxidation mechanism in photosystem II, including oxidations, proton release pathways, O–O bond formation and O_2 release. Biochim. Biophys. Acta. 2013; 1827:1003–1019. [PubMed: 23103385]
22. Rivalta I, Brudvig GW, Batista VS. Oxomanganese complexes for natural and artificial photosynthesis. Curr. Opin. Chem. Biol. 2012; 16:11–18. [PubMed: 22481113]
23. Debus RJ, Strickler MA, Walker LM, Hillier W. No evidence from FTIR difference spectroscopy that aspartate-170 of the D1 polypeptide ligates a manganese ion that undergoes oxidation during the S_0 to S_1, S_1 to S_2, or S_2 to S_3 transitions in photosystem II. Biochemistry. 2005; 44:1367–1374. [PubMed: 15683222]
24. Pushkar Y, Yano J, Sauer K, Boussac A, Yachandra VK. Structural changes in the Mn_4Ca cluster and the mechanism of photosynthetic water splitting. Proc. Natl Acad. Sci. USA. 2008; 105:1879–1884. [PubMed: 18250316]
25. Dau H, Zaharieva I, Haumann M. Recent developments in research on water oxidation by photosystem II. Curr. Opin. Chem. Biol. 2012; 16:3–10. [PubMed: 22387134]
26. Wampler RD, et al. Selective detection of protein crystals by second harmonic microscopy. J. Am. Chem. Soc. 2008; 130:14076–14077. [PubMed: 18831587]
27. Weierstall U, Spence JCH, Doak RB. Injector for scattering measurements on fully solvated biospecies. Rev. Sci. Instrum. 2012; 83:035108. [PubMed: 22462961]
28. Dekker JP, Plijter JJ, Ouwehand L, Vangorkom HJ. Kinetics of manganese redox transitions in the oxygen-evolving apparatus of photosynthesis. Biochim. Biophys. Acta. 1984; 767:176–179.
29. Karplus PA, Diederichs K. Linking crystallographic model and data quality. Science. 2012; 336:1030–1033. [PubMed: 22628654]
30. Sauter NK, Hattne J, Grosse-Kunstleve RW, Echols N. New Python-based methods for data processing. Acta Crystallogr. D. 2013; 69:1274–1282. [PubMed: 23793153]
31. Kok B, Forbush B, McGloin M. Cooperation of charges in photosynthetic O_2 evolution-I. A linear four step mechanism. Photochem. Photobiol. 1970; 11:457–475. [PubMed: 5456273]
32. Zouni A, Jordan R, Schlodder E, Fromme P, Witt HT. First photosystem II crystals capable of water oxidation. Biochim. Biophys. Acta. 2000; 1457:103–105. [PubMed: 10773155]
33. Han G, et al. Direct quantification of the four individual S states in photosystem II using EPR spectroscopy. Biochim. Biophys. Acta. 2008; 1777:496–503. [PubMed: 18406339]
34. Han G, Mamedov F, Styring S. Misses during water oxidation in photosystem II are S state-dependent. J. Biol. Chem. 2012; 287:13422–13429. [PubMed: 22374999]
35. Weierstall U, et al. Droplet streams for serial crystallography of proteins. Exp. Fluids. 2008; 44:675–689.
36. DePonte DP, et al. Gas dynamic virtual nozzle for generation of microscopic droplet streams. J. Phys. D Appl. Phys. 2008; 41:195505.
37. Lomb L, et al. An anti-settling sample delivery instrument for serial femtosecond crystallography. J. Appl. Cryst. 2012; 45:674–678.

38. Philipp HT, Hromalik M, Tate M, Koerner L, Gruner SM. Pixel array detector for X-ray free electron laser experiments. Nucl. Instrum. Methods Phys Res. A. 2011; 649:67–69.
39. Herrmann S, et al. CSPAD-140k: a versatile detector for LCLS experiments. Nucl. Instrum. Methods Phys Res. A. 2013; 718:550–553.
40. de Wijn R, van Gorkom HJ. Kinetics of electron transfer from Q_A to Q_B in photosystem II. Biochemistry. 2001; 40:11912–11922. [PubMed: 11570892]
41. Kirian RA, et al. Femtosecond protein nanocrystallography–data analysis methods. Opt. Express. 2010; 18:5713–5723. [PubMed: 20389587]
42. McCoy AJ. Solving structures of protein complexes by molecular replacement with Phaser. Acta Crystallogr. D. 2007; 63:32–41. [PubMed: 17164524]
43. Read RJ. New ways of looking at experimental phasing. Acta Crystallogr. D. 2003; 59:1891–1902. [PubMed: 14573943]
44. Afonine PV, et al. Towards automated crystallographic structure refinement with phenix.refine. Acta Crystallogr. D. 2012; 68:352–367. [PubMed: 22505256]
45. Bhat TN. Calculation of an OMIT map. J. Appl. Cryst. 1988; 21:279–281.
46. Vellieux FMD, Dijkstra BW. Computation of Bhat's OMIT maps with different coefficients. J. Appl. Cryst. 1997; 30:396–399.
47. Emsley P, Lohkamp B, Scott WG, Cowtan K. Features and development of Coot. Acta Crystallogr. D. 2010; 66:486–501. [PubMed: 20383002]
48. Hodel A, Kim SH, Brunger AT. Model bias in macromolecular crystal structures. Acta Crystallogr. A. 1992; 48:851–858.
49. Terwilliger TC, et al. Iterative-build OMIT maps: map improvement by iterative model building and refinement without model bias. Acta Crystallogr. D. 2008; 64:515–524. [PubMed: 18453687]
50. Cox N, Pantazis DA, Neese F, Lubitz W. Biological water oxidation. Acc. Chem. Res. 2013; 46:1588–1596. [PubMed: 23506074]
51. Grundmeier A, Dau H. Structural models of the manganese complex of photosystem II and mechanistic implications. Biochim. Biophys. Acta. 2012; 1817:88–105. [PubMed: 21787743]
52. Yano J, Yachandra VK. Where water is oxidized to dioxygen: structure of the photosynthetic Mn_4Ca cluster from X-ray spectroscopy. Inorg. Chem. 2008; 47:1711–1726. [PubMed: 18330965]
53. Siegbahn PE. Substrate water exchange for the oxygen evolving complex in PSII in the S_1, S_2, and S_3 states. J. Am. Chem. Soc. 2013; 135:9442–9449. [PubMed: 23742698]
54. Yamaguchi K, et al. The nature of chemical bonds of the $CaMn_4O_5$ cluster in oxygen evolving complex of photosystem II: Jahn-Teller distortion and its suppression by Ca doping in cubane structures. Int. J. Quantum Chem. 2013; 113:453–473.
55. Kanady JS, Tsui EY, Day MW, Agapie T. A synthetic model of the Mn_3Ca subsite of the oxygen-evolving complex in photosystem II. Science. 2011; 333:733–736. [PubMed: 21817047]
56. Yano J, Yachandra VK. Oxidation state changes of the Mn_4Ca cluster in photosystem II. Photosynth. Res. 2007; 92:289–303. [PubMed: 17429751]
57. Chu HA, Nguyen AP, Debus RJ. Amino acid residues that influence the binding of manganese or calcium to photosystem II. 1. The lumenal interhelical domains of the D1 polypeptide. Biochemistry. 1995; 34:5839–5858. [PubMed: 7727445]
58. Hundelt M, Hays AM, Debus RJ, Junge W. Oxygenic photosystem II: the mutation D1–D61N in *Synechocystis* sp. PCC 6803 retards S-state transitions without affecting electron transfer from Y_Z to P_{680}+ Biochemistry. 1998; 37:14450–14456. [PubMed: 9772171]
59. Dilbeck PL, et al. The D1–D61N mutation in *Synechocystis* sp. PCC 6803 allows the observation of pH-sensitive intermediates in the formation and release of O_2 from photosystem II. Biochemistry. 2012; 51:1079–1091. [PubMed: 22191538]

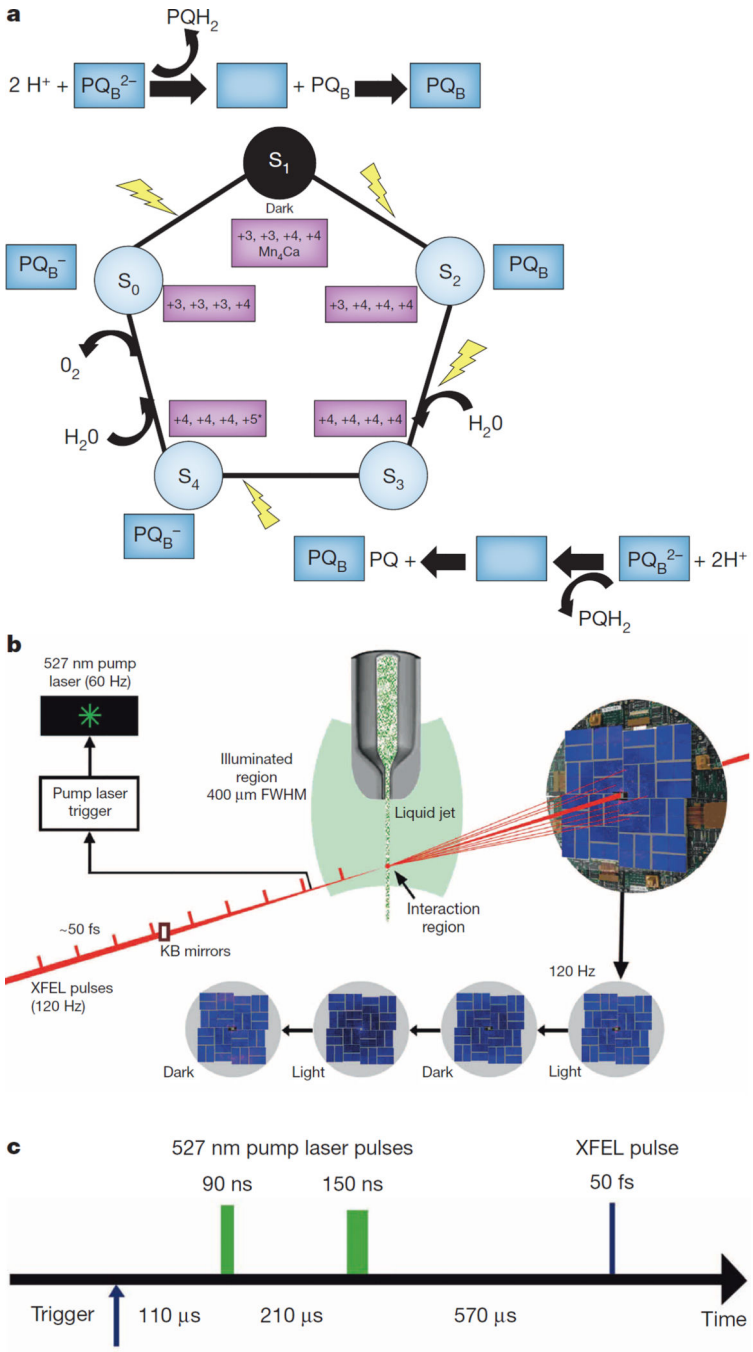

Figure 1. Experimental schemes for the time-resolved serial femtosecond crystallography experiments on photosystem II

a, S-state scheme of the oxygen-evolving complex depicting changes the oxidation state of the 4 manganese ions of the Mn_4CaO_5 cluster in the S-state cycle (*note that the oxidation states of the Mn atoms in the S_4 state are still under debate). The scheme also indicates the reduction of the plastoquinone (PQ) to plastoquinol (PQH_2) in the Q_B site. The blank boxes represent the unoccupied PQ_B binding site. **b**, Experimental setup. The crystal-stream of photosystem II, was exposed to two subsequent optical laser pulses at 527 nm before interacting with the femtosecond X-ray FEL pulses. With a FEL frequency of 120 Hz and

triggering of the laser at 60 Hz, X-ray diffraction patterns from crystals in the dark state and ‘light’ double-flash state alternate. **c**, Laser excitation scheme. The first 527 nm laser pulse excited the crystals 110 μs after the trigger pulse. The delay time between the first and second 527 nm laser pulse was 210 μs, with X-ray diffraction data collected 570 μs after the second laser pulse.

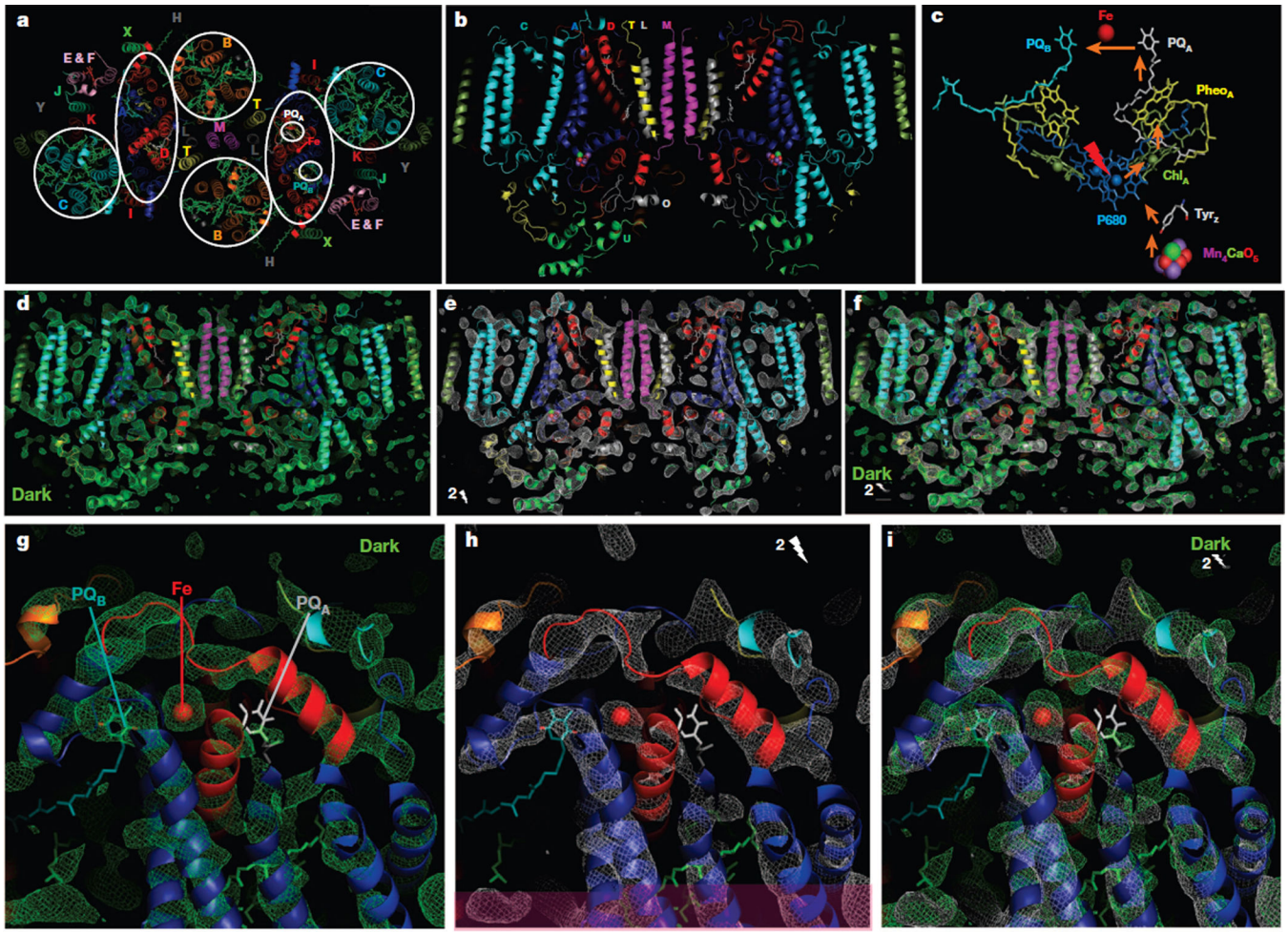

Figure 2. Overall structure and omit map electron density of photosystem II

a, Transmembrane helices and cofactors in photosystem II (stromal view density map). The proteins are named according to their genes and labelled with coloured letters. **b**, Side view of PSII at its longest axis along the membrane plane. **c**, Electron transport chain of PSII (P680 (blue), accessory chlorophylls (olive-green), pheophytins (yellow) and plastoquinones PQ_A (white) and PQ_B (cyan)); atoms of the OEC are depicted as spheres (Mn purple, Ca green, Olight red). **d**–**f**, Omit map electron densities (view as in **b**) at 1.5 σ for the dark state (S_1) (green) (**d**), double-flash state (putative S_3 state) (white) (**e**) and overlay of the two omit maps (**f**). **g**–**i**, Omit maps (1.5 σ) of the electron acceptor side of photosystem II for the dark (S_1) (green) (**g**), double-flash (putative S_3 state) (white) (**h**) and overlay of the two omit maps (**i**). Note that changes include a shift of the electron density of the non-haem iron.

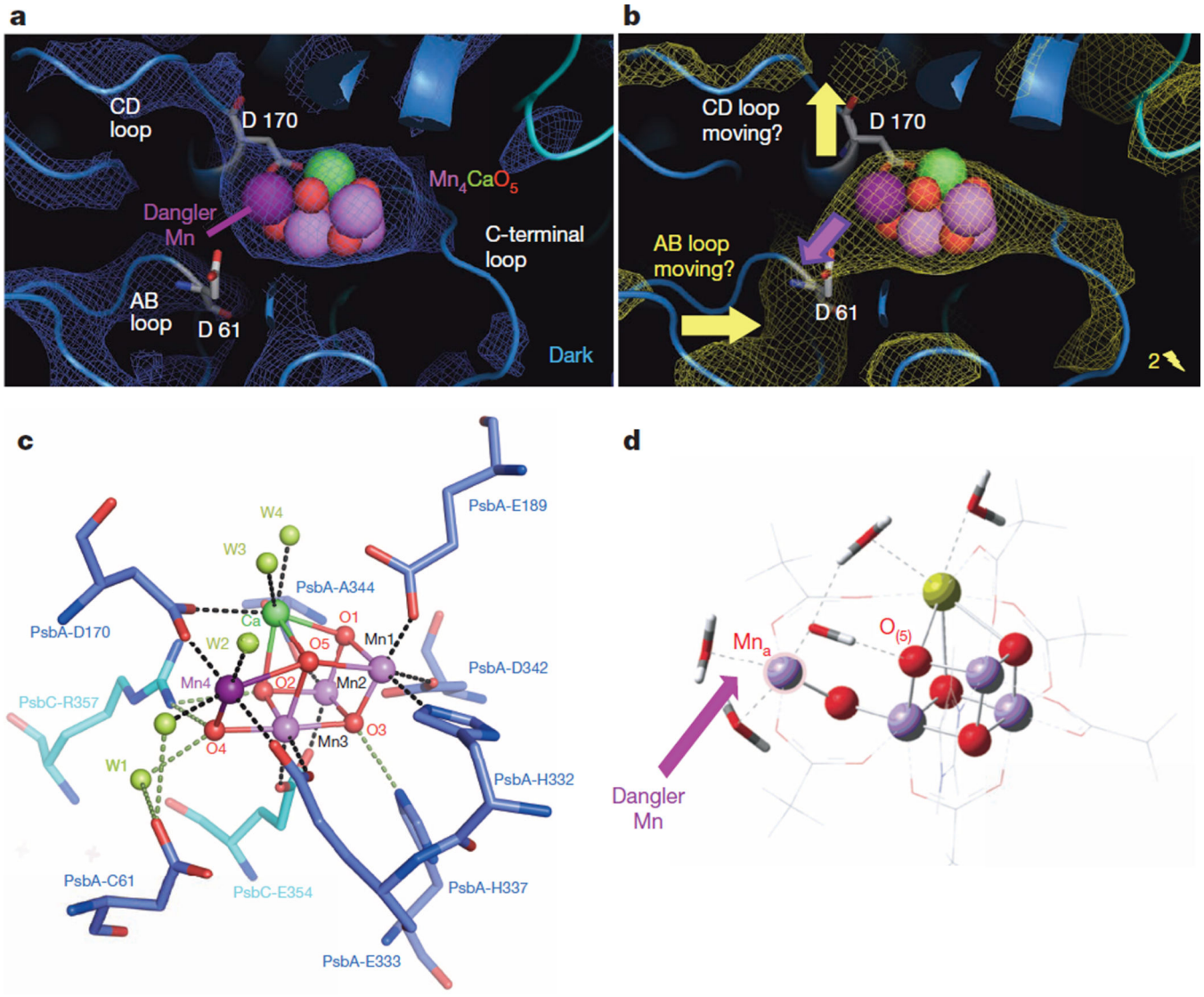

Figure 3. The OEC simulated annealed omit maps

a, **b**, At 1.5 σ for dark and double-flash states of the Mn_4CaO_5 cluster of PSII for the dark S_1-state (blue) (**a**) and double-flash, putative S_3 state (**b**) with the 1.9 Å structural model (3ARC) from ref. 6. Mn in the distorted Mn_3O_xCa cubane (Mn-1 to Mn-3) (light-pink), dangler manganese (Mn-4) (violet), calcium (green) and oxygen (red). **c**, 1.9 Å crystal structure of the Mn_4CaO_5 cluster with ligands from ref. 6 (PDB accession code: 3ARC). **d**, Proposed model of the S_3 state based on DFT calculations by Isobe *et al.*[4] (reproduced with permission of The Royal Society of Chemistry). Larger diversions in the SA-omit map of the double-flash (putative S_3 state) include potential movement of the loop connecting transmembrane helices C/D (CD loop) with D170 and AB loop (with D61), and an increase of the distance between the dangler Mn and the Mn_3O_xCa cubane (violet arrow).

Table 1

Statistics of the dark (S_1) and double-flash (putative S_3) data sets collected at CXI, LCLS

	Dark data set	Double-flash data set
Wavelength (Å)	2.05	2.05
Resolution range (Å)	100.6–5.0	102.3–5.5
Space group	$P2_12_12_1$	$P2_12_12_1$
Unit cell length (Å)	133.3 ± 1.6, 226.3 ± 2.1, 307.1 ± 3.1	136.6 ± 1.5, 228.1 ± 2.3, 308.7 ± 3.8
Total reflections	28,679,554 (1,679,683)	12,476,013 (1,018,721)
Unique reflections	40,946 (2,710)	32,066 (2,651)
Multiplicity	700.35 (618.0)	388.55 (381.1)
Completeness (%)	99.98 (100)	99.88(100)
Mean I/σ (I)	10.65 (2.1)	8.03(1.75)
$CC_{1/2}$ *	0.914 (0.740)	0.877 (0.635)
R_{split}	0.07 (0.37)	0.09 (0.49)
R_{work}	0.260 (0.3502)	0.280 (0.3820)
R_{free}	0.262 (0.3434)	0.290 (0.3477)
RMS† (bonds)Å	0.039	0.039
RMS† (bonds) deg	3.029	3.029
Number of atoms	49,817	49,817
Protein residues	5,214	5,214
Ramachandran favoured† (%)	97.7	97.7
Ramachandran outliers† (%)	0.2	0.2
Clashscore (Molprobity)	5.5	5.8
Mean B-factor‡ (Å^2)	33.7	33.7

$$R_{\text{split}} = \sqrt{2}\frac{\sum_{hkl}|I_{\text{even}} - I_{\text{odd}}|}{\sum_{hkl}|I_{\text{even}} + I_{\text{odd}}|}$$ See Extended Data Fig. 4 for a comparison of R_{split} vs resolution.

Numbers in parentheses refer to values for the highest resolution shell.

*$CC_{1/2}$ is Pearson's coefficient calculated as described in ref. 29.

†The values for the RMS for bonds and angles as well as the Ramachandran values are positively biased by the high resolution model with PDB accession code 3ARC.

‡The B-factors were taken from the high resolution model with PDB accession code 3ARC and not refined.